Fabrication and Evaluation of Multiple Memory Nitinol Stents for Biomedical Applications

by

Gitanjali Shanbhag

A thesis
presented to the University of Waterloo
in fulfillment of the
thesis requirement for the degree of
Master of Applied Science
in
Mechanical and Mechatronics Engineering

Waterloo, Ontario, Canada, 2017

Author's Declaration

I hereby declare that I am the sole author of this thesis. This is a true copy of the thesis, including any required final revisions, as accepted by my examiners.

I understand that my thesis may be made electronically available to the public.

Abstract

Cardiovascular diseases (CVD) are the leading cause of deaths worldwide. The development of stents led to a revolutionary phase in the treatment of these diseases [1]. A stent is a tubular metallic structure that is implanted within an artery during an angioplasty procedure to give on-going support in the form of scaffolding to maintain blood vessel patency [2]. The unique properties of nitinol such as pseudoelasticity, shape memory, excellent biocompatibility, and corrosion resistance, make it a highly desirable material for fabrication of stents. The superelastic properties of nitinol stents allow good self-expansion ratio and uniform radial expansion with less longitudinal shortening. These properties promote the use of nitinol for stenting through the development of self-expanding stents [3]–[9].

Conventional fabrication processes for NiTi stents limit their performance since only a constant pseudoelastic (PE) force can be achieved along the length. However biological systems rarely have constant forces (i.e. radial), hence variable PE force would allow the design and fabrication of a more compatible device. This work focusses on locally modifying the pseudoelasticity of NiTi stents to enable conformity to the surrounding biological system. This was achieved through the application of a high-power density laser that locally modifies the microstructure for predetermined locations along the tube. Subsequently, it was found that the laser processed tube exhibited altered PE properties as compared to the original base material. The mechanism behind this pseudoelastic force modification is the effect of the replacement of a portion of the base metal by a series of laser processed zones.

Three-point bend tests, tensile tests and stent crush tests were carried out to demonstrate the localized control and customization of the stent's thermomechanical properties. Finally, the laser

processed stents were fabricated and evaluated both thermally and mechanically and compared to a base material stent. Although more work is needed to understand the exact deformation mechanisms, this method offers precise pseudoelastic force tuning for stents by changing the material properties, which, until now has not been possible. There does not yet exist a stent that has ideal properties that would make its use optimal for all cases. Every design influences the blood-stent interactions differently [10].

Acknowledgements

I would like to thank my supervisors Dr. Norman Zhou and Dr. Mustafa Yavuz for their guidance and advice throughout my research. Their constant motivation and encouragement has helped me achieve this degree.

I would also like to thank the current and past employees of Smarteralloys: Ibraheem Khan, Siu Kei Tang, Andrew Pequegnat as well as my colleague Andrew Michael for always helping and being available for advice.

Finally, I would like to thank my parents, my grandparents and my brother for their encouragement and endless support during my studies.

This work has been supported by Smarteralloys, Ontario Centres of Excellence (OCE) and the Natural Science and Engineering Research Council of Canada (NSERC).

Dedication

To my loving mom who is a constant source of inspiration

Table of Contents

List of Figures

List of Tables

Chapter 1: Introduction

1.1. Background

The remarkable properties of Nickel – Titanium (NiTi) shape memory alloys (SMAs) such as the shape memory effect (SME), Pseudoelasticity (PE), high strength, good corrosion resistance, excellent biocompatibility, etc. makes them a highly desirable material for medical implants [11]–[14]. The SME allows the alloy to recover its original shape by the application of thermal energy, even after large deformation approaching 10% strain. The PE of SMAs allows for large recoverable strains (upto 8% in polycrystalline materials) simulating many of the mechanical responses in the human body, such as the hair, bone, and tendons [14], [15]. One medical implant of considerable interest is a stent, which is a metallic mesh tube that is mounted in a catheter and inserted into the blood vessel to counteract the effects associated with plaque growth inside an artery. The catheter releases the stent after which the stent self-expands at body temperature, compresses the plaque, and exerts a radial force on the arterial walls to keep it open. Conventional fabrication processes for NiTi stents produce homogeneous pseudoelastic properties throughout the device which is a limitation in case of an arterial vessel that has a region of plaque - healthy lumen zone – plaque. The healthy vessel wall does not need as much radial force and hence there should be a variable radial force across the length of the stent. The constant PE force exhibited by stents can limit the design and functionality, which is of importance for biological systems that are complex with varying geometric features. The ability to locally tune the properties along a monolithic stent can enable us in achieving variable forces. The Multiple Memory Material (MMM) technology is a recent development that can embed multiple properties in a monolithic

NiTi component [16]. This technology can be used to embed and locally tune the properties along a monolithic stent and enable better patient outcomes.

1.2. Objective

The objective of this thesis is to investigate an approach towards demonstrating the ability to modify the pseudoelasticity (PE) of a monolithic NiTi stent and comparing the mechanical properties to an untreated stent. The specific objectives include:

1) Investigation of the effects of partial penetration laser processing on phase transformation characteristics and mechanical properties

2) Development of the ability to modify the PE of Nitinol stents by adjusting the laser processing parameters

3) Demonstration of the capability of achieving high quality laser cutting of the multiple memory material (MMM) as a stent material

1.3. Thesis Outline

This thesis is divided into five parts. Chapter 2 presents a review of existing literature relating to the functional properties of SMAs, laser processing, use of NiTi SMAs as stent material and fundamentals of laser cutting of stents. Chapter 3 describes the fabrication process of the NiTi stents and how laser processing embeds the multiple memory material technology. In Chapter 4, the effect of laser processing on the mechanical performance of these stents is discussed. Finally, the main conclusions drawn from the results of this study as well as recommendations for future work are presented in Chapter 5.

Chapter 2: Literature Review

Introduction

The first half of this chapter provides a detailed review of the existing literature associated with stents for the treatment of cardiovascular disease, use of NiTi as a stent material and NiTi shape memory alloys. The second half introduces fundamentals of laser processing of NiTi and laser cutting for NiTi stents to understand the basic process characteristics, important parameters and essential factors typically considered.

2.1 Stents for the treatment of cardiovascular disease (CVD)

The aorta is the largest artery in the human body. It extends from the left ventricle of the heart and carries oxygen-rich blood for distribution throughout the body via an intricate system of small and branched arteries. The right and left coronary arteries supply blood for the heart muscles (shown in Figure 1). Severe narrowing and blockage (stenosis) of these arteries can cause angina pectoris (chest pain) or heart attack. Coronary artery disease is a buildup of fat and cholesterol, also known as plaque (shown in Figure 2), in these main arteries, restricting blood flow as these passageways gradually narrow and, in some cases, become completely obstructed. This disease claims more than 7 million lives worldwide every year [17] . According to the World Health Organization (WHO) estimates, in 2005, cardiovascular diseases have accounted for 30% of all deaths globally. Cardiovascular stents are used as vessel scaffolding to assuage an arterial narrowing or stenosis and restore blood flow in these narrowed and blocked arteries. A stent is a tube-like scaffold that can be dilated using a balloon (balloon-expandable) or on its own (self-expandable) to achieve a customized fit within narrowed arteries following plaque removal, where it serves as a critical support against the closing of weak arteries [18], [19]. Cardiovascular diseases, continue to be a

major problem, causing abundant untimely deaths worldwide. The underlying motivation of this work is to improve the clinical outcome of stents. From the perspective of the clinical use, a stent must fulfil several mechanical criteria, and stent manufactures are trying to address these by improving stent designs.

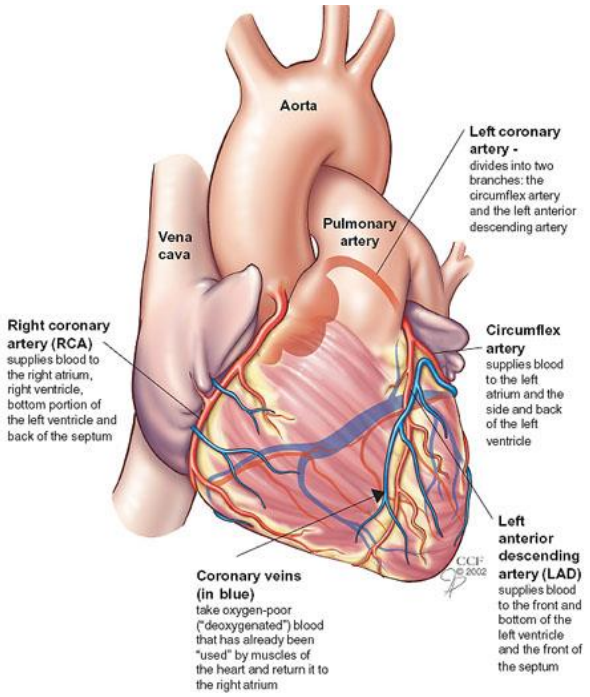

Figure 1 Schematic representation of the Aorta and the branching arteries [20]

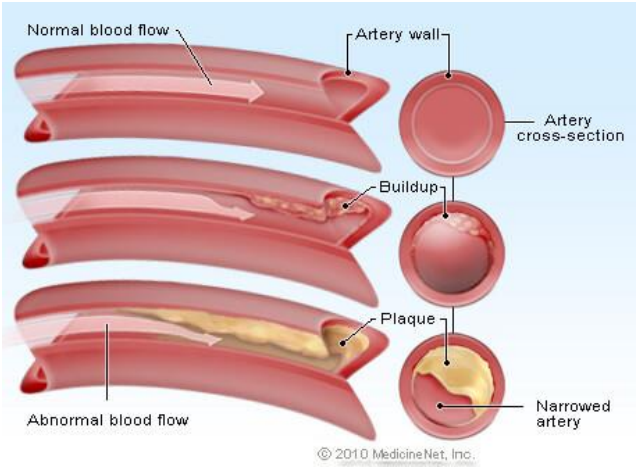

Figure 2 Schematic of an artery clogged with plaque [21]

Since their inception in the mid 1980s, stents have gained popularity in the medical community because they allow diseased vessels to be treated using minimally invasive surgical (MIS) techniques thereby reducing the trauma, cost and many complications associated with traditional surgery. Generally, stenting is performed on arteries that are diagnosed to have narrowed beyond an allowable percentage of the normal arterial diameter. A stent is preloaded onto a catheter, in a collapsed form, and enters the vascular system through the femoral or radial arteries [22]. Further on, this collapsed stent is advanced distally through the convoluted vascular system and delivered to the region of the narrowed artery and expanded within the vessel. Upon expansion, stents undergo radial expansion and longitudinal recoiling, i.e., increase in the radius, and decrease in the length. Hence, this should be considered while designing the stent. The size of the plaque formed and targeted vessel for deployment define the diameter and length of the stent to be implanted.

2.1.1 Stent Design

The basic design of a stent includes an array of repeating elements known as struts. Struts are disposed around the circumference of a stent, and joined together. The union of adjacent struts is termed as an apex. A series of struts and apices that spans one complete circumference is termed as a ring. Adjacent rings of struts are joined by connectors which connect some or all apices forming pattern. The long-term stability of the stent depends on the device supporting the vessel wall and promoting the reinstitution of a healthy blood vessel. The above-mentioned terms are depicted in Figure 3. The depiction is just used for explanation of terms and is not the stent design used for the current work.

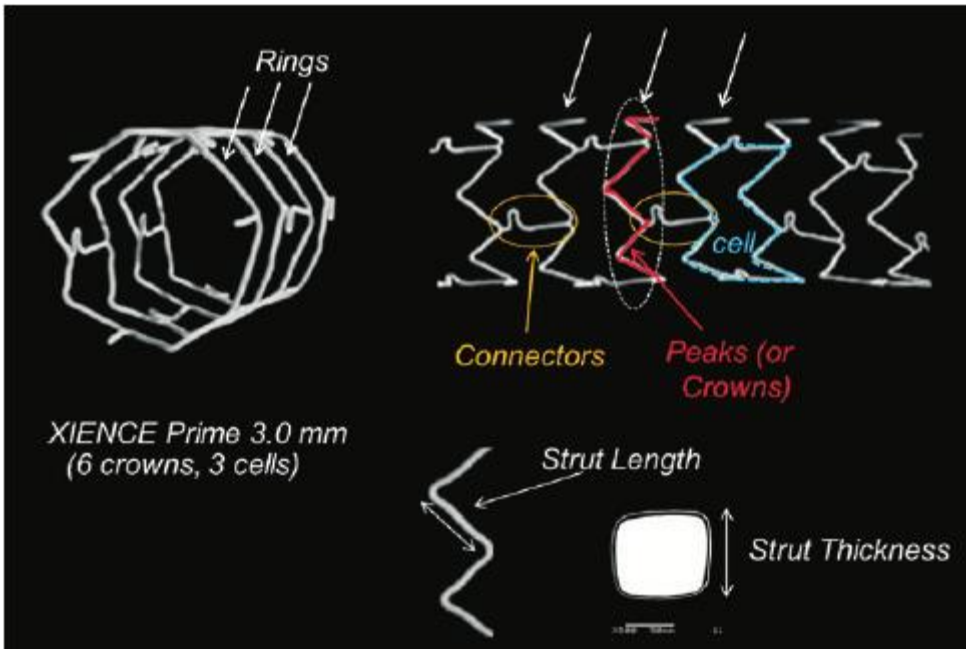

Figure 3 Schematic showing the key features of a stent [23]

Commercially available stents are categorized in the followings ways;

(a) by method of deployment,

(b) by strut pattern,

(c) by material used

Based on the method of deployment, stents are classified as balloon expandable stents or self-expandable stents [24]. Balloon expanding (BX) stents are manufactured in the crimped state and expanded to the vessel diameter by inflating a balloon and plastically deforming the stent. Self-expanding (SX) stents are manufactured at the required vessel diameter or slightly above and are constrained to a smaller diameter until the intended delivery site is reached where the stent is deployed and expands [24]. The stent-to-artery diameter ratio is 1.1 to 1.2 times the diameter of

the blood vessel in order to ensure that the stent is securely fastened to the vessel walls [25]. In the expanded form, the stent should have radial rigidity and recoil control [26], [27]. SX stents are the most widely chosen category. The most widely used material is NiTi, which can recover elastic deformations of up to 10% (large elastic strain and low elastic modulus) [19].These stents have no strength limitation and elastically recover after complete radial crushing as opposed to BX stents that can collapse if a critical external pressure is exceeded. A BX stent is stiffer than an SX stent because of the low elastic modulus of SX stents (NiTi stents), therefore, the radial compliance of an SX stented vessel is greater than that of a BX stented vessel [24].

Based on the strut patterns, the stents are classified into open-cell design stents and closed-cell design stents. The number and position of connectors between the cells differentiate the two designs. Closed-cell designs describe a ring where bridge elements connect all internal inflection points. The advantage of this design is that it provides uniform scaffolding to support the vessel walls. Open-cell designs have fewer bridge connectors allowing more flexibility due to a reduced amount of connection points between adjacent sections. They also have large intrastrut areas as compared to the closed-cell designs. This design offers better conformability to vessel curvature, however, a higher incidence for protrusion of intimal tissue or plaque in between struts has been reported, which might highly impact the performance of the stent [28], [29].

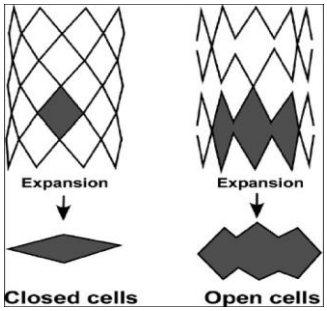

Figure 4 Schematic of an open cell and closed cell design [28]

As shown in Figure 4, with the closed cell design, cell geometry connects consistently throughout. Upon expansion, the individual cells do not merge to form larger open areas. With the open cell design, cell geometry does not connect consistently throughout forming incomplete bridges and hence upon expansion, the individual cells merge to form larger open areas [28].

Stent materials are chosen based on their properties such as strength, corrosion resistance or radiopacity. Biocompatible materials such as stainless steel, nitinol, titanium, and cobalt-chromium, are commonly used for stents [30].

A stent is always designed to improve the in vivo performance and reduce restenosis and damage to the interior surface of blood vessels, mainly due to the expansion of the stent in the arterial wall. In an investigation performed by Garcia et. al. [31] it has been stated that the response of the artery to the high pressure of the stent on the arterial walls leads to endothelial damage which may cause cell proliferation and restenosis. The study also shows that a variable radial force (VF) stent is required to decrease the pressure effects in the healthy areas of the arterial wall that remains in contact with the stent, along with avoiding the possible restenosis in the diseased part of the wall. They achieved a VF stent model by changing geometrical parameters in an already present commercial stent design (Acculink, Abbott Vascular). A comparison of the VF stent and constant force (CF) stent for the same design reveals that the VF design shows the possibility of limiting the high contact pressure areas in healthy lumen zones of a diseased vessel along with maintaining constant radial strength in the stenotic part. The figure below shows the contact pressure distribution along the arterial walls for the CF and VF stents that have some amount of plaque causing stenosis. The reduction in high pressures in the healthy areas relative to the central part (plaque region) of the VF stent model can be seen in Figure 5 (b), meanwhile the distribution of

the pressure is more continuous and with higher values for the case of the CF stent (Figure 5 (a)). The reduction in these pressures (Figure 5 (b)) also translate to better performance in the diseased part of the arterial wall along with minimising the risk of damaging the healthy part of the arterial wall.

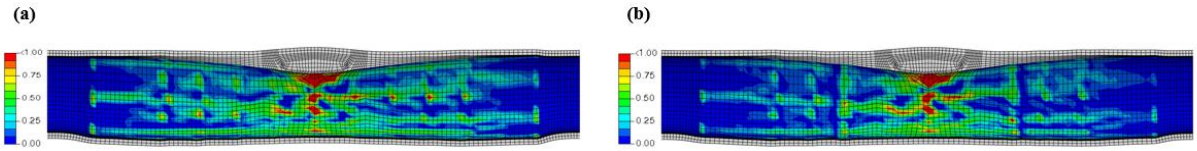

Figure 5 Contact pressure distribution [MPa] for the stenotic vessel for (a) CF stent (b) VF stent [31]

Although, a limitation of this study is that results have been obtained for only one stent commercial design (Acculink, Abbott Vascular). Another limitation could be the fact that, during the modelling of the vessel, the plaque was introduced as radially eccentric and longitudinally symmetric. Varying from patient to patient, the plaque might not be symmetric onto the walls of the vessel. Also, there might be multiple simultaneous regions of plaque-healthy areas-plaque and so on.

A schematic of a region of plaque surrounded by healthy lumen zones is shown in Figure 6.

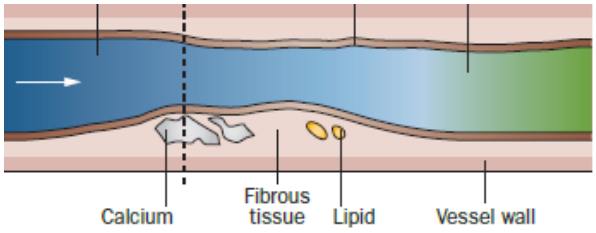

Figure 6 Schematic of an artery with calcification and small lipid pools. The plaque leads to mild narrowing of the lumen in the centre although there are healthy regions at the ends of the artery (adapted from [32]*)*

Hence, a stent that can be modified in a way that there is more than one region where the force can be modified, can be beneficial. For this study, nitinol has been chosen as the stent material due to

the tunability of its localised mechanical properties, which can prove to be beneficial for our application and will be discussed further in Section 2.3 Laser Processing of NiTi SMA.

2.1.2 Use of Nickel-Titanium (NiTi) as a stent material

Traditionally, most stents were built from stainless steel. Unfortunately, stainless steel is not fully biocompatible and implantation is usually followed by restenosis and thrombosis. In addition, stainless steel can pose difficulties related to magnetic resonance imaging [33], [34]. Materials for stents should exhibit large elastic strains. Nitinol is one of very few alloys that is pseudoelastic, biocompatible, exhibits large elastic strains, easily trackable, etc. These properties are discussed in this section, with respect to usage of NiTi as a stent material. An appropriate discussion of SME and PE can be found in section 2.2.3 Functional Properties of SMAs.

(i) Biocompatibility & Biomechanical Compatibility - In 1986, the consensus of a U.K. conference *Definitions in Biomaterials* defined biocompatibility as "the ability of a material to perform with an appropriate host response in a specific application [35]" Nitinol has excellent biocompatibility, due to the formation of a passive titanium-oxide layer (TiO2) [36], [37]. The oxide layer increases the stability of the surface layers by protecting the bulk material from corrosion and also creates a chemical barrier against Ni oxidation [38].

The extraordinary conformity of nitinol makes it most mechanically similar to biological materials (Figure 7) like hair, tendon and bone, which can be elastically deformed, and in some cases deformation up to 10% strain can take place [39].

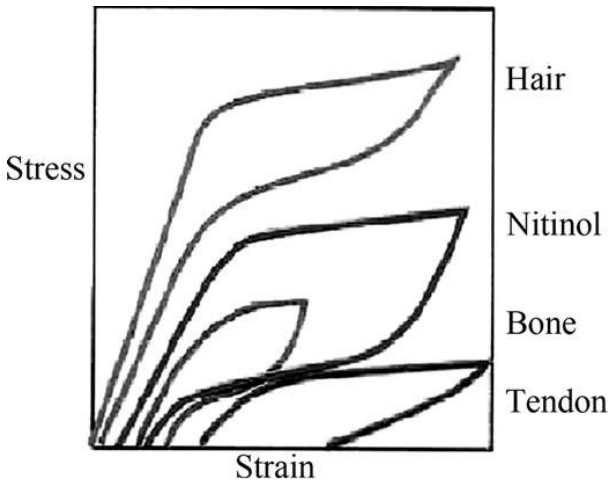

Figure 7 Loding and unloading curves for Nitinol and living tissues [39]

(ii) Magnetic Resonance (MR) Compatibility – With the increased use of Magnetic Resonance Imaging procedures, MR compatibility is an essential requirement for implants. Nitinol is non-ferromagnetic with a lower magnetic susceptibility than stainless steel. MRI compatibility is directly related to the susceptibility of a material relative to human tissue. Therefore, nitinol provides a clear image, with much less artifacts as compared to stainless steel [11], [33].

(iii) Stress Hysteresis – In most engineering materials, stress increases linearly with strain upon loading and decreases upon unloading along the same path. Although in nitinol, an initial linear increase in stress with strain is observed. Large strains can be obtained with only a small further stress increase. This is known as the loading plateau and the end of this plateau is reached at about 8% strain. Unloading from the end of the plateau region, causes the stress to decrease rapidly until a lower plateau (unloading plateau) is reached. Strain is recovered in this region with only a small decrease in stress. The last portion of the deforming strain is finally recovered in a linear fashion. This stress hysteresis in a device is termed as biased stiffness [40], [41].

In Figure 8, a stent of a given size (point a), is compressed/crimped into the delivery system (point b). Upon release from the delivery system inside the vessel it expands (from point b), following the unloading path of the stress/strain curve. At point c, it reaches the diameter of the vessel lumen, positioning itself against the vessel wall with a low outward force or chronic outward force (COF). This force remains nearly constant even when the vessel increases in diameter. If there is a recoil pressure due to spasms or external compression, the stent resists deformation with a greater force or radial resistive force (RRF) as shown by the loading curve from c to d which is steeper than the unloading line (towards e). In this way the stress hysteresis of NiTi allows the design of stents with biased stiffness, meaning that the stents exert small outward force but resist deformation with a much greater force [40], [42]. Thus, the above discussion supports the fact that nitinol has become the ideal material for fabrication of stents.

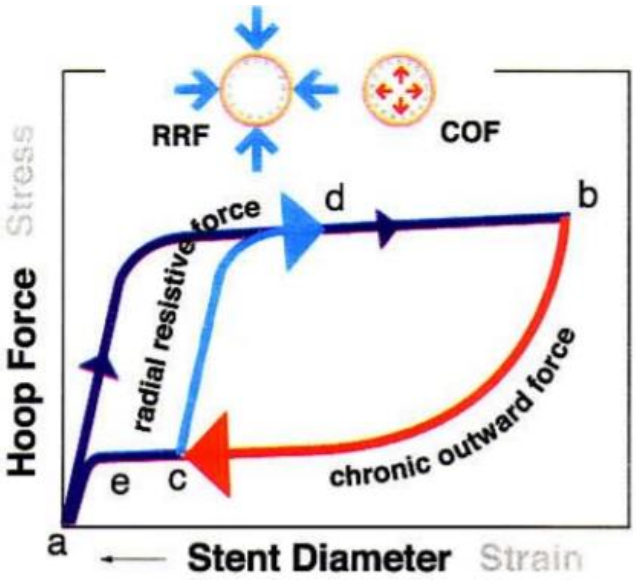

Figure 8'Biased stiffness' of stents as a result of stress hysteresis in NiTi [40]

2.2 Nickel-Titanium (NiTi) Shape Memory Alloys

NiTi shape memory alloy is a binary nickel titanium alloy with near equiatomic composition [13].

Discovered in 1958 as part of a Naval research project [43], Nitinol derives its name from its chemical components and its founders: Ni (Nickel) + Ti (Titanium) + NOL (Naval Ordinance Lab). Since its commercial introduction in the 1970s, Nitinol has been used for a variety of applications: pipe couplings, eyeglass frames, orthodontic wires, mobile phone antennas, micro-actuators, earthquake dampeners, etc. [11], [44]. Recently, however, the Nitinol community's trend has been to turn its efforts to the biomedical device field [14], [40].

2.2.1 Phases in NiTi SMAs

NiTi SMAs are considered an organised intermetallic compound (IMC) [13]. Figure 9 depicts the binary phase diagram for the Ni-Ti system. Our region of interest is the central region bounded by Ti_2Ni and $TiNi_3$ phases. At room temperature, there is no solubility of constituent species and the SMA exists as a stoichiometric IMC. However above 630°C, Ni becomes soluble in Ti to form NiTi [45]. To form NiTi, the molten alloy must be quenched within the soluble range (labelled in Figure 9). Nitinol's first-order phase transformation progresses from the parent austenite, a simple cubic B2 (CsCl) structure, to the daughter martensite, monoclinic B19' phase, via an athermal transformation [46]. The austenite B2 (CsCl) type ordered structure has a lattice constant of 0.3015 nm at room temperature whereas the martensite monoclinic B19' crystal structure has lattice parameters a = 0.2889, b = 0.4120 and c = 0.4622 and monoclinic angle $\beta = 96.8°$ [47]. An intermediate R-phase is observed in materials that have undergone thermomechanical treatments to increase the dislocation density, form Ni-rich precipitates, or form nanocrystalline grains [48]–[50]. The R-phase has a rhombohedral crystal structure and appears under certain conditions prior to the transformation to B19' phase.

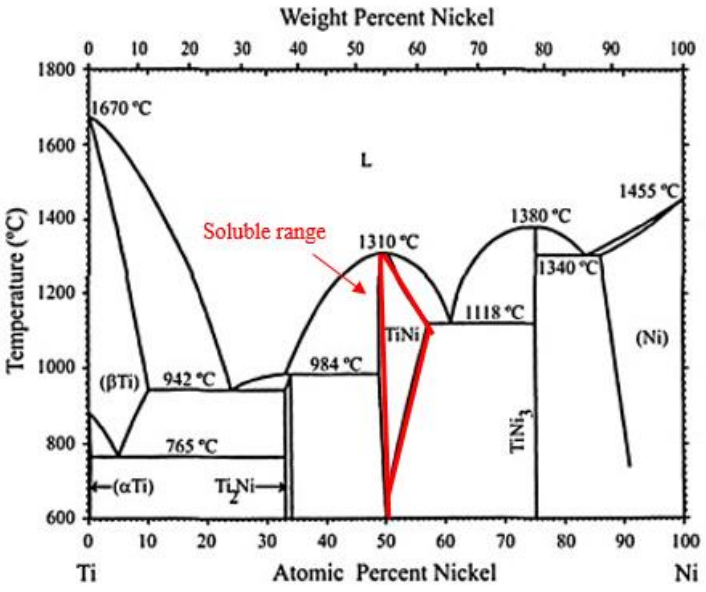

Figure 9 Binary phase diagram of NiTi with the soluble range highlighted [51]

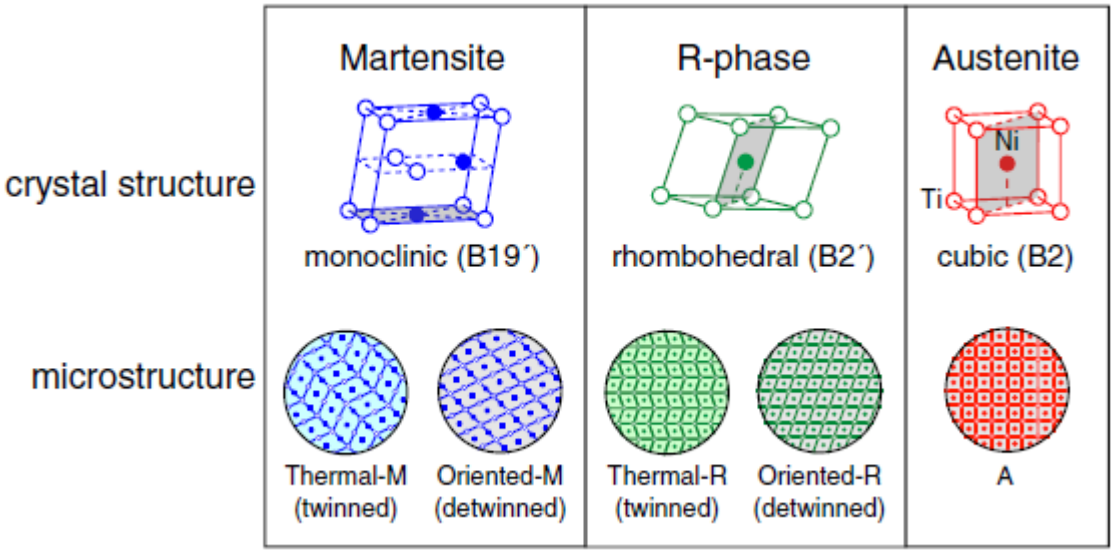

Figure 10 Three distinct phases of NiTi SMA's: Martensite, Austenite, R-phase [52]

2.2.2 Martensitic Phase Transformation in NiTi SMAs

The crystallographic lattice during martensitic transformations is accompanied by a shear deformation, which can alter the volume and shape of the material. Martensitic transformation can

take place at low temperatures, because it requires no diffusion [53]. Martensitic transformation in steel alloys is accommodated by irreversible dislocation motion however, in SMAs, reversible martensitic transformations are accommodated by twinning of the underlying microstructure [54], [55]. The accommodation in volume and shape change can take place through slipping or twinning (illustrated in Figure 11). Slipping involves gliding of the atomic planes over high energy slip planes, creating irreversible dislocation and change in the crystal lattice. FCC and BCC lattices are prone to slip due to a higher availability of slip systems and high stacking fault energies. Twinning on the contrary is the shearing of the crystal lattice where the structures on each side of the habit plane are a mirror. Twinning occurs in NiTi SMAs due to lack of symmetry and available slip systems [56].

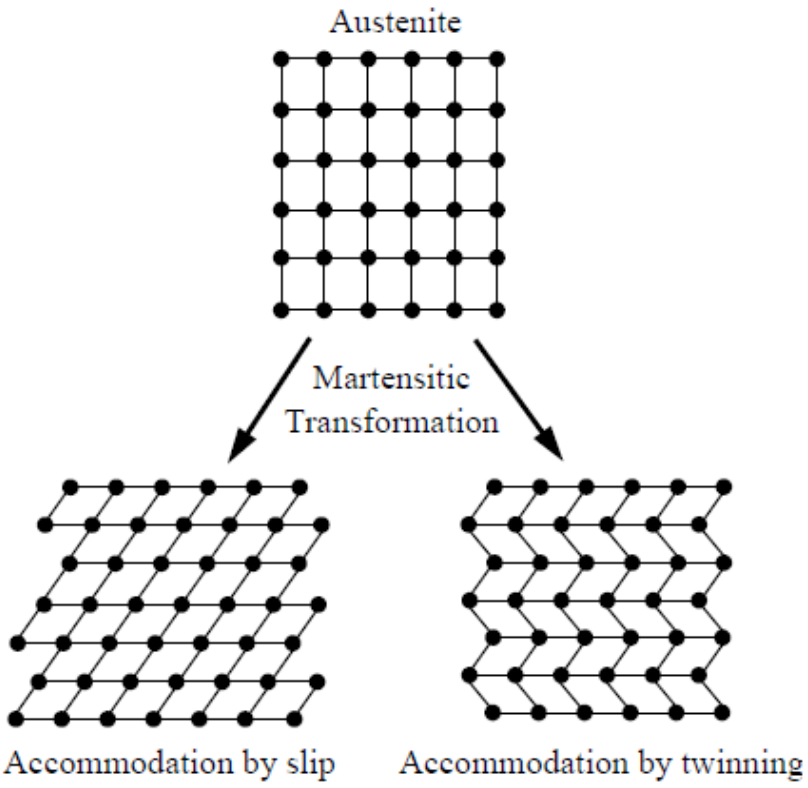

Figure 11 Martensitic Phase Transformation by slip and twinning [57]

There are three different paths for martensitic transformations in NiTi SMAs as shown in Figure 12. The first transformation path is from B2 to orthorhombic B19 martensite and finally to monoclinic B19' martensite. This transformation is observed only in the case of NiTiCu alloys with Cu above 7.5 at% [58]. The second path is the thermoelastic martensitic transformation from cubic B2 austenite to monoclinic B19' martensite. This transformation is observed in NiTi alloys that have either been solution treated or possess only low amounts of cold work or precipitation [13]. The third path is from cubic B2 to trigonal R phase and finally to monoclinic B19' martensite. The R-phase forms when the B19' transformation is either suppressed by the Fe alloying element, dislocations created through cold work or Ni-rich precipitates following aging treatment [59].

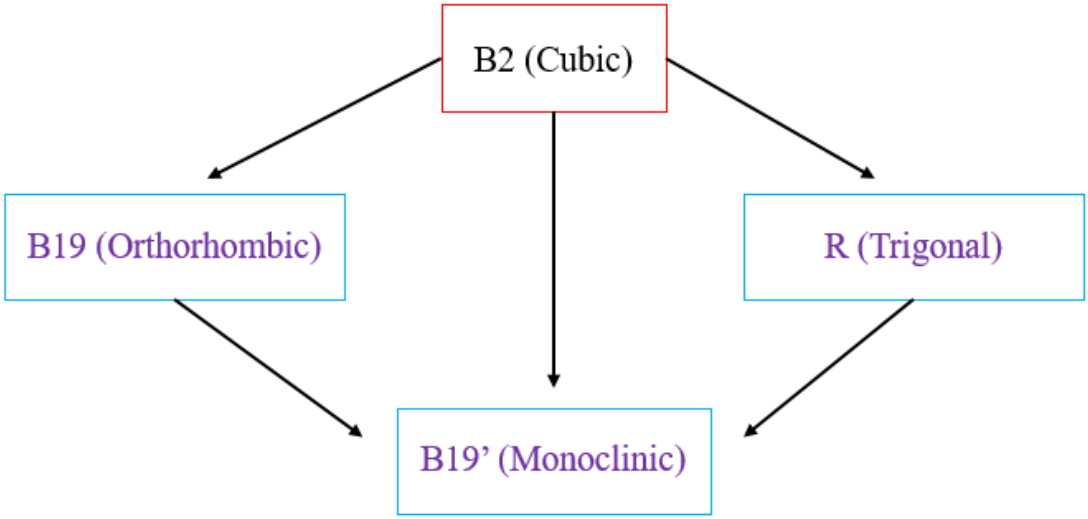

Figure 12 Three possible transformation paths for NiTi alloys [13]

2.2.3 Functional Properties of SMAs

The functional properties of SMAs originate from the thermomechanical response of the material. The thermomechanical response of NiTi SMAs can be differentiated into two properties depending on whether the austenite ↔ martensite transformation is induced thermally or by applied stress.

Thermally induced transformation enables the shape memory effect (SME) while the stress induced transformation leads to pseudoelasticity (PE) [54], [55], [57].

2.2.3.1 Shape Memory Effect

The transformation from austenite to martensite and the reverse transformation from martensite to austenite do not take place at the same temperature. The following four temperatures characterize the complete transformation cycle: austenite start temperature (A_s), austenite finish temperature (A_f), martensite start temperature (M_s) and martensite finish temperature (M_f). If a mechanical load is applied to the material in the twinned martensitic phase, detwinning is possible by reorientation of a certain number of variants. The detwinning process results in a macroscopic shape change, where the deformed configuration is retained upon unloading as shown in Figure 13. A subsequent heating of the SMA to a temperature above A_f will result in a reverse phase transformation (from detwinned martensite to austenite) and will lead to complete shape recovery (see Figure 13). This process is defined as the Shape Memory Effect (SME) [55], [60].

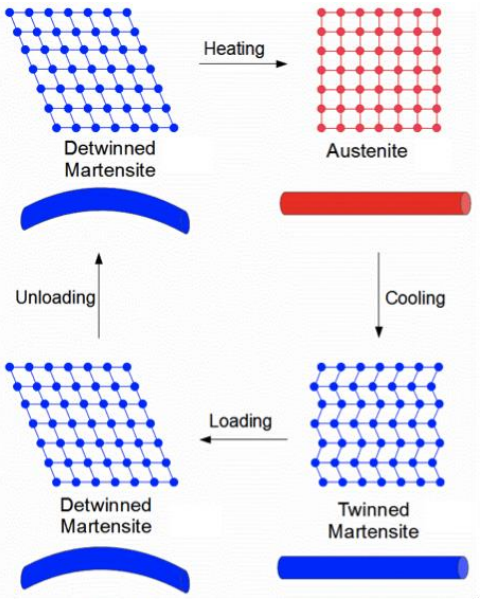

Figure 13 Illustration of Shape Memory Effect in NiTi SMAs [61]

The transformation temperatures can be characterized by the Differential Scanning Calorimetry (DSC) technique. A typical DSC plot for a NiTi alloy is presented in Figure 14. A distinct hysteresis in the phase transformation temperatures when transforming from martensite to austenite opposed to from austenite to martensite is observed. This hysteresis results from internal friction and defects in the crystal structure [62].

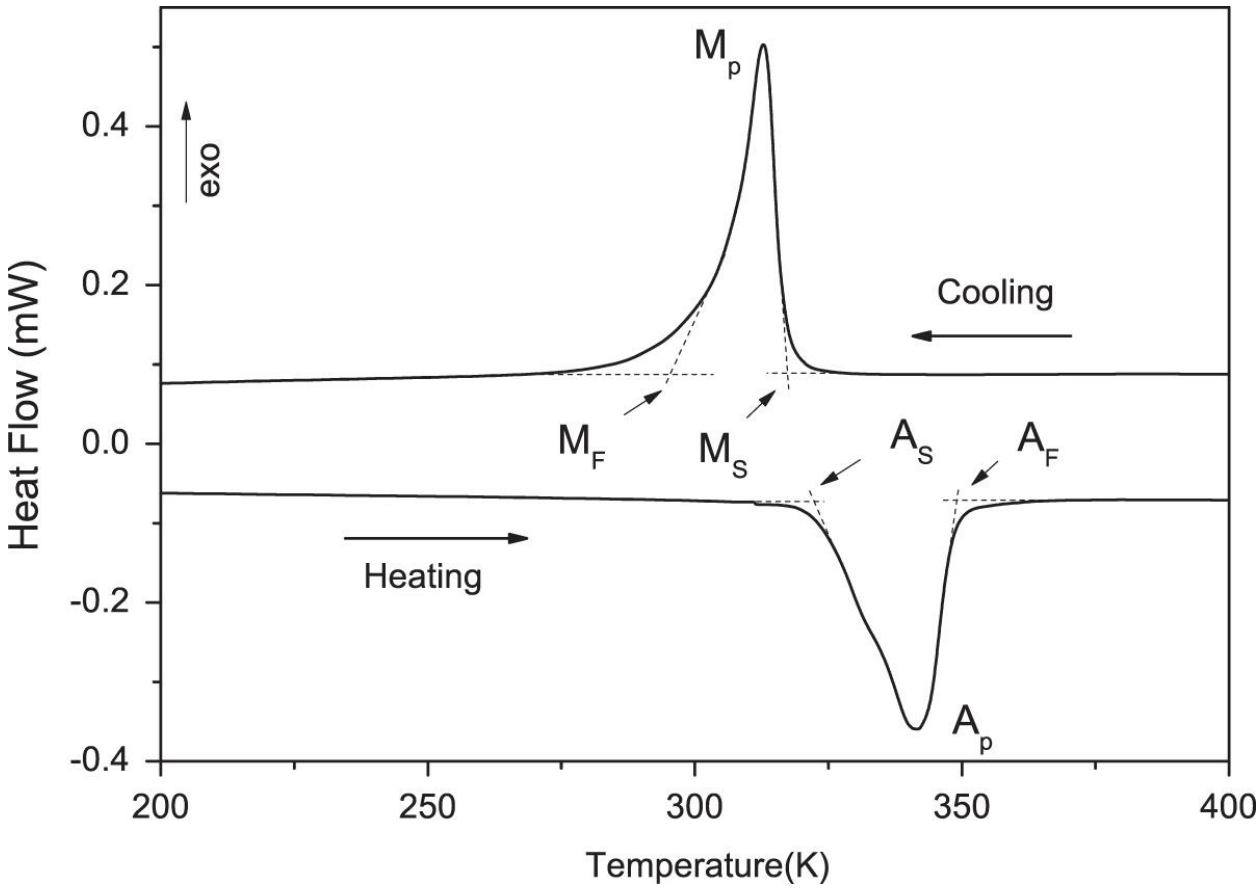

Figure 14 A typical DSC Curve for NiTi SMAs [63]

2.2.3.2 Pseudoelasticity

The pseudoelastic behavior is exhibited when austenite transforms to stress-induced martensite (SIM), which leads to strain generation during loading and subsequent strain recovery upon unloading at temperatures above A_f. A pseudoelastic thermomechanical loading path generally starts at a high temperature where austenite is stable, then develops under an applied load to a state at which detwinned martensite is stable, and finally returns to the austenitic phase when returned to zero stress state [55]. Pseudoelastic behaviour is generally characterized by tensile testing. A typical cyclic tensile curve is shown in Figure 15.

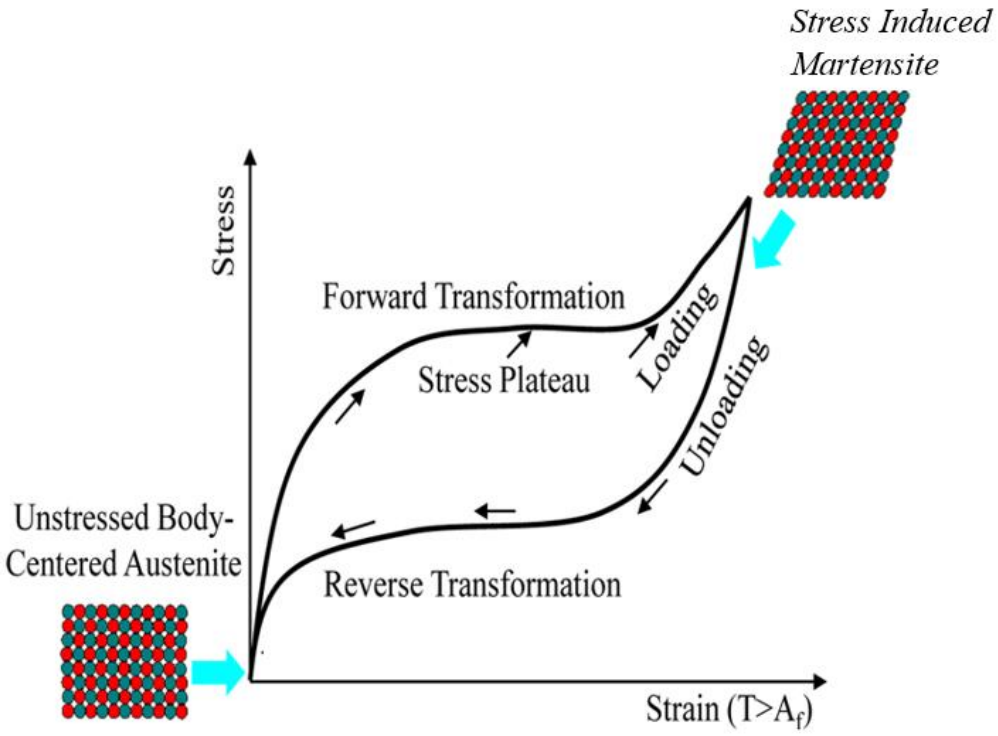

Figure 15 Tensile curve depicting how stress varies with strain during a reversible elastic deformation [64]

Initially the material is in the austenitic phase (Figure 15). At a certain load, the austenite phase starts to shear into SIM in an isostress fashion, following a Lüders-like deformation in which a

shear band propagates across the specimen [65]. Upon complete SIM transformation, the SIM again deforms in typical linear elastic manner. Finally, at the end of the unloading path the material is again in the austenitic phase. As the temperature of NiTi increases above A_f, the thermodynamic stability of austenite phase also increases. The linear relationship between tensile stress and temperature is derived from the Clausius-Clapeyron equation [66]:

$$\frac{\partial \sigma}{\partial T} = \frac{-\Delta H}{T\varepsilon_0}$$

where $\partial\sigma$ is the change in plateau stress, T is the test temperature, ΔH is the latent heat of transformation (obtained from DSC measurements), and $\boldsymbol{\varepsilon}_0$, is the transformational strain. ΔH and $\boldsymbol{\varepsilon}_0$, are controlled by the crystallography of the transformation and can be considered constants. This equation highlights the importance of understanding the material behaviour at the in-service temperature of an SMA device.

Figure 16 illustrates the temperatures at which SME and PE are exhibited. Below A_s the SME occurs with applied stress, whereas above A_f, PE is observed. The critical stress for slip of the material must be above the critical stress for stress induced martensite (A); otherwise the material would plastically deform before stress induced martensite is formed (B). The temperature at which the stress for slip is less than the stress for stress induced martensite is called the M_d temperature and is indicated in Figure 16. Above M_d, the austenite is mechanically stable. In the temperature regime between As and A_f the martensite is partly unstable, and thus both superelasticity and shape memory effects coexist [13].

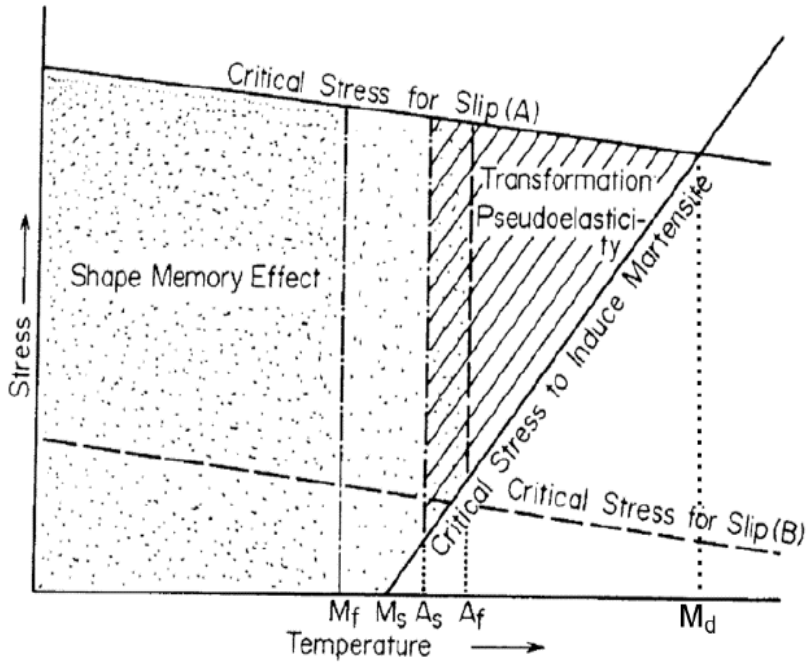

Figure 16 Regions of activity for SME and PE in NiTi SMAs [67]

2.2.4 Laser Processing in NiTi SMA

The term "laser" was originated as an acronym for light amplification by stimulated emission of radiation [68], [69]. Arthur Schawlow and Charles Towns first published the concept of laser. Their theoretical work led to the invention of the first working ruby laser by Theodore Maiman in 1960 [70]. Table 1 shows the wavelength bands and radiation spectrum covered by commercial lasers. After commercialisation of lasers, they found applications into various fields such as optical disk drives, laser printers and barcode scanners, DNA sequencing instruments, fiber-optic and free-space optical communication, laser surgery and skin treatments, cutting and welding materials; military and law enforcement devices for marking targets and measuring range and speed, etc. Many applications from these fields involve material processing using lasers which resulted in stimulating the creation and further development of research activities in the area of laser materials processing [69], [71], [72].

Table 1 Range of wavelengths for current commercial lasers [69]

Laser type	Lasing species	Principle wavelength (μm)	Region	Date invented/commercialised
Excimer	F_2	0.157	UV	1975/1976
	ArF	0.193	UV	
	KrF	0.248	UV	
Nd:YAG frequency-quadrupled	$Nd^{3+} \times 4$	0.266	UV	
	XeCl	0.308	UV	
	XeF	0.351	UV	
Nitrogen	N_2	0.337	UV	1966/1969
AlGaN diode	Band gap	0.38–0.45 (tunable)	Blue	
Helium–cadmium	Cd^+	0.4416	Blue	1968/1970
Argon	Ar^+	0.4880	Blue	1964/1966
	Ar^+	0.5145	Green	
Copper vapour	Cu*	0.5106	Blue-green	1966/1981
	Cu*	0.5782	Yellow	
Nd:YAG frequency-doubled	$Nd^{3+} \times 2$	0.532	Green	
Helium–neon	Ne*	0.6328	Red	1962
Ruby	Cr^{3+}	0.6943	Red	1960/1963
Alexandrite	Cr^{3+}	0.700–0.820 (tunable)	IR	1977/1981
Ti:sapphire	Ti^{3+}	0.670–1.100 (tunable)	IR	
AlGaAs diode	Band gap	0.7–0.9 (tunable)	IR	1962/1965
Nd:YAG or Nd:glass	Nd^{3+}	1.064	IR	1964/1966
Yb:YAG or Yb:glass	Yb^{3+}	1.030	IR	1990s
Chemical oxygen–iodine	Chemical ($O_2 + I_2$)	1.3	IR	1964/1983
Er:YAG	Er^{3+}	1.5	IR	
Hydrogen fluoride	Chemical ($H_2 + F_2$)	2.6–3.0	IR	1967/1977
Helium–neon	Ne*	3.39	IR	
Carbon monoxide	CO vibration	5.4	IR	
Carbon dioxide	CO_2	9.4	IR	
	vibration	10.64	IR	1964/1966
Dye	Fluorescence	1.1–0.3 (tunable)	IR–UV	1962/1965
Free electron	Electron vibration	12.0–0.1 (tunable)	IR–UV	1963/1969

Lasers are common sources of energy for welding and cutting of SMAs due to localized heat input and high cooling rates [73]. When a high-energy density source such as a laser strikes the surface of NiTi alloy, preferential vaporization of Ni takes place. This preferential vaporization occurs due to the higher equilibrium vapour pressure of Ni as compared to Ti (as shown in Figure 17). The vaporization of Ni due to laser processing, leads to a change in the local composition of the alloy from Ni-rich to Ti-rich [74]. The functional properties of NiTi SMAs are extremely sensitive to changes in composition. This is due to the phase transformation temperatures being extremely sensitive to the mole fraction of Ni, as shown by Tang [75] and Frenzel et al. [76] in Figure 18. A slight change of composition drastically changes the transformation temperature. Thus, the laser processed zones (LPZs) have correspondingly higher phase transformation temperatures with increasing Ti composition, shown in Figure 19 [74].

The extreme dependence of the physical properties of NiTi on the composition and the microstructure leads to significant changes in local material properties after laser processing. This allows for the origination of monolithic NiTi components with various properties [74], [77]. Recently, considerable interest has been shown in the performance improvement of NiTi SMAs with laser processing on its biocompatibility [78] and functional properties. Efforts have been focused on creating a change in local composition in a single SMA device. Technologies such as the multiple memory technology [79] and laser annealing [80] have proven to transform the way SMA devices are designed. Through localized control over NiTi composition, multiple memories can be embedded and programmed in a single monolithic piece of SMA and thus a change in the functional, mechanical and biocompatibility properties is expected. Although literature suggests that the yield strength and working strains are reduced following laser processing [81]–[85]. The

effects of past material treatments such as cold work, precipitation hardening, etc. are lost following the thermal cycles induced by the laser process [81], [84], [85].

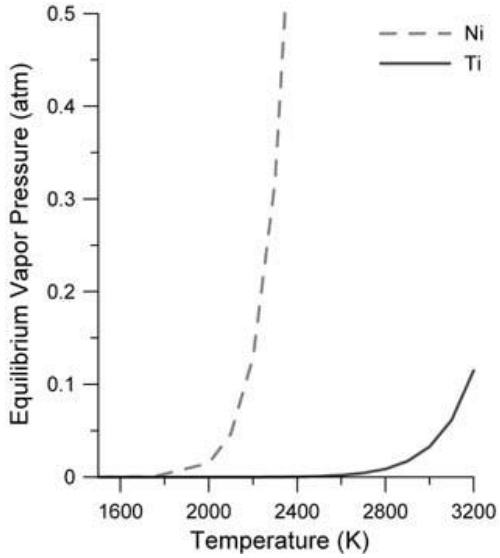

Figure 17 Calculated vapour pressures of Nickel and Titanium for an equiatomic NiTi alloy. Ni has significantly higher vapour pressure than Ti at the same temperature [74]

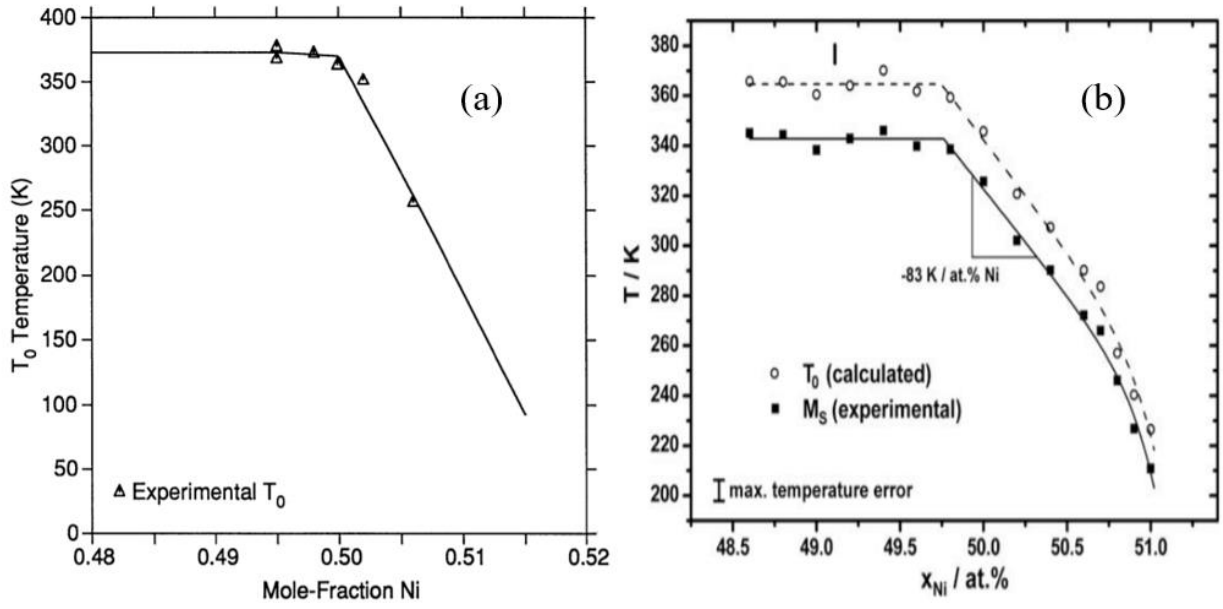

Figure 18 Relation between mole-fraction of Ni and M_s temperature in binary NiTi SMAs a) by Tang [75] *and b) by Frenzel et al.* [76]

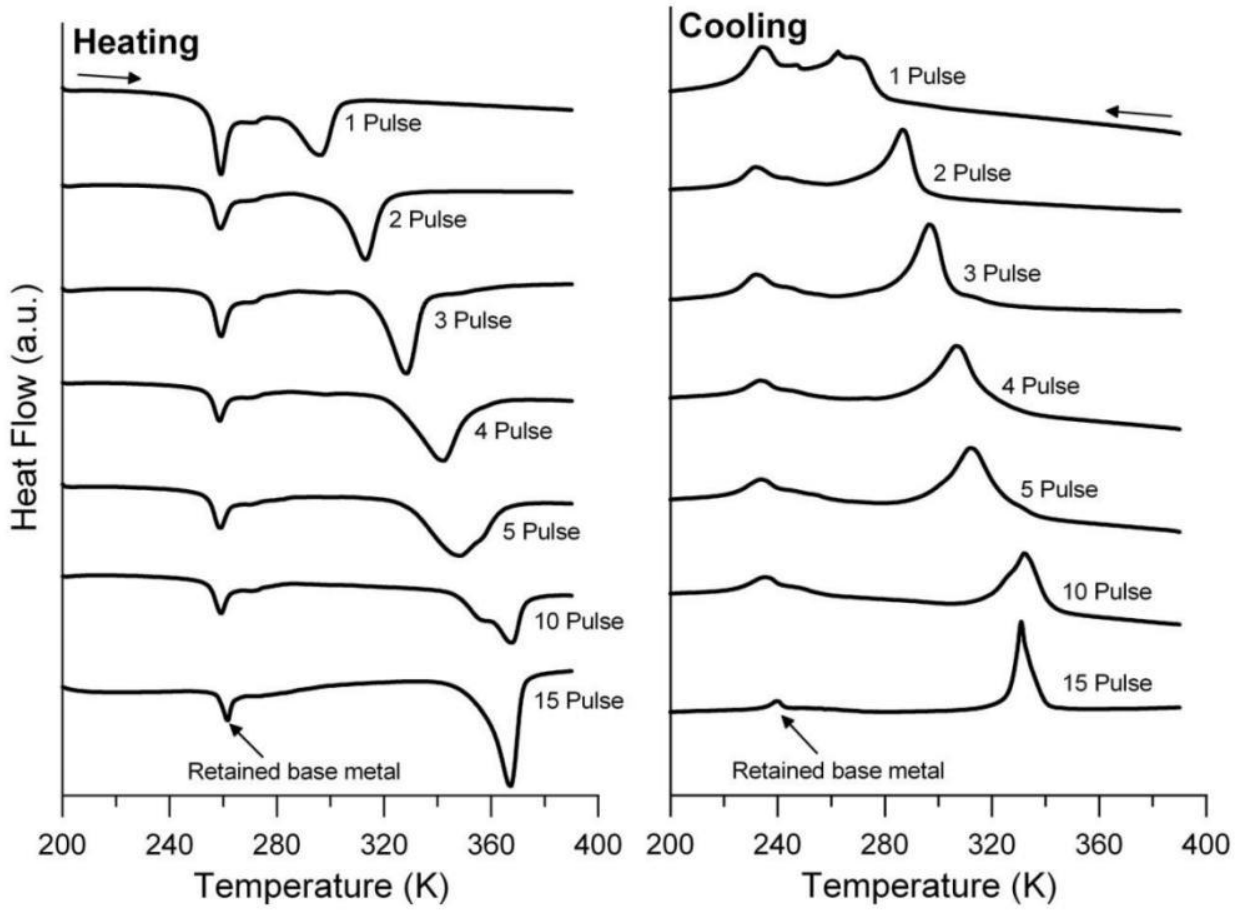

Figure 19 DSC analysis of laser pulse processing of Ti-50.7 at%. Ni alloy wire. A second set of phase transformation peaks is identified at higher temperatures in both the heating (B2→B19') and cooling (B19'→B2) curves. These peaks correspond to the laser processed sections [74]

The main goal of the current work is to study the influence of laser processing on a self-expanding NiTi stent and to use it towards improving the blood vessel – stent device interaction by using them to advance towards a variable radial force stent. This can be achieved by the application of a high-power density laser that locally modifies the microstructure for predetermined locations along the tube. Subsequently, the laser processed tube exhibits altered PE properties as compared to the original base material and hence modifies the pseudoelasticity of these regions in the stent to enable conformity to the surrounding biological system.

2.3 Laser cutting of stents

One of the growing applications of lasers in biotechnology and biomedical engineering is the laser cutting of stents. Stenting refers to the practice of bracing traumatized or diseased tubular vessel walls in the human body to: a) increase the diameter and thereby the flow through the tube, and/or b) so that the vessels do not collapse due to their own inherent weakness [30], [86], [87]. The demanding design requirements for stents dictate the need for high precision and accuracy while fabricating these devices. In 1994, the first laser cut stent (Palmaz-Schatz stent) for clinical practice was approved in the United States [88].

2.3.1 Fabrication processes for Stents

Stent fabrication is a technique that requires proficiency in many fields, starting from the selection of raw material, through high-precision cutting of complex geometries, to perfect finishing to ensure the highest quality of the desired product. Laser cutting is used as the fabrication process for NiTi stents for this thesis, although a brief description of some of the other techniques for cutting of the complex stent geometries is also provided below.

(i) Wire braiding or knitting

Braiding wire into a tubular mesh configuration is achieved in this process. One such stent which is commercially available is the Wallstent. The device is described in the patent WO-A-83/03752. It consists of two sets of counter-rotating helical filaments of metallic wire which are braided together in a one over/one under pattern [89]. A distinct limitation of the braided or knitted stents is the crossing of the filaments. It increases the wall thickness of the stent and the delivery profile. A second disadvantage is the possibility of fretting corrosion and the wear of the stent material at

the cross-over points [40]. The braided fabrication technique also allows relative sliding and rotation between wires which might lead to alteration of the geometry [90].

(ii) Photochemical Etching

Photo chemical machining or etching is a manufacturing process that uses photoresist film and highly concentrated acid to dissolve metal in controlled areas to produce parts and textures. The process of implantable stent fabrication works by chemically machining a complex stent pattern onto flat sheet material. This pattern can then be heat set or rolled to form a tube shape [91], [92]. Certain disadvantages of this process are the handling of dangerous chemicals, disposal of potentially harmful by-products and the metal removal rate may be slow and non-uniform.

(iii) Water jet cutting

The supersonic water jet travels across a mixing chamber to enter a nozzle-shaped focusing tube, where it collimates into a narrow energetic cutting beam. As the beam impinges on the target, a combination of erosion mechanisms removes material. Different erosion phenomena prevail depending on what type of material is being targeted. A drawback of this technique is that that precision cutting can only be obtained if the fine abrasive water jet is manipulated at adequate precision. Also, geometries might be limited by the cutting width in this process [93], [94].

(iv) Laser cutting

Laser cutting is a process in which a high intensity laser beam is used to rapidly heat the target, subsequently melting the material through full depth of the target [95]. Figure 20 depicts a schematic and principle of a laser cutting process. A focussing lens narrows the laser beam down to a smaller spot. Small spot size is preferred during the cutting process for a precise material removal and high accuracy. A conical nozzle with assist gas is usually employed coaxial with the

laser. The introduction of assist gas is to enhance the ejection of the molten materials out of the kerf [95][96]. Some of the advantages of the laser cutting process are: ease of automation with computer numerical control (CNC) and robotic processing, which provides systematic control over the dimensions and speed which is highly favorable for cutting complex designs; small spot size (down to a few micron) that offers high geometric accuracy and precision; high cutting speed which improves productivity[97]–[100].

Currently laser cutting requires post processing to produce high quality stents. The surface quality of stent plays a major role since it has a significant influence on biocompatibility. There are a few methods for post-processing such as acid pickling. Pickling technique is performed by immersing the stent in a tank containing the following mixture: HCl=7%, $FeCl_2$ = 8% and balance H_2O [101]. The other method to replace acid pickling is by applying soft etching. This involves electrochemical etching with a weak acid. Electropolishing is a post-processing treatment which is performed, after the samples have undergone acid pickling and heat-treatment processes, to obtain a sufficiently smooth surface of stents. Electropolishing is the process of enhancing and smoothing the surface of stents in an electrolyte solution containing H_2SO_4 (95-97%), H_3PO_4 (85 wt.%) and H2O (balance)[102], [103] . To protect against the harmful release of nickel into the human body, Electropolishing is required to create a protective titanium oxide layer. Although post-processing is out of the scope of the current study and hence has not been performed.

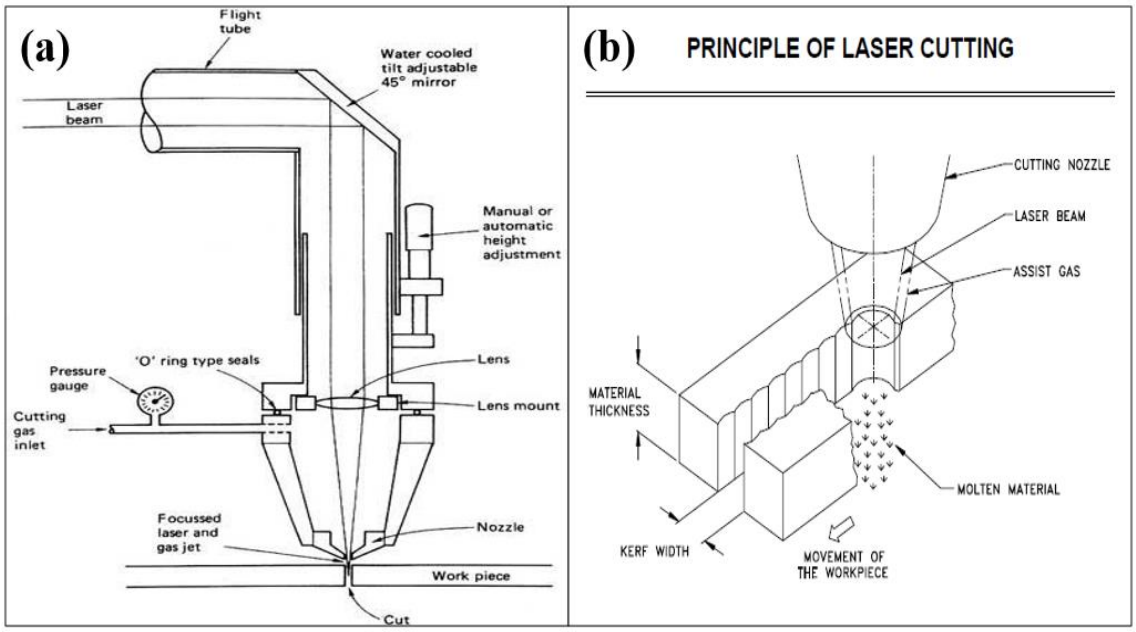

Figure 20 (a) Schematic depicting the laser cutting process [96] *(b)Schematic explaining the principle of laser cutting* [104]

2.3.2 Factors influencing laser cutting

Of importance in the application of laser cutting technology, is to increase productivity, quality of cutting surface and material savings. Experimental studies have shown that, to achieve these goals it is necessary to consider many influential parameters. This section discusses the effects of some of the most important laser-cutting parameters on the geometric and metallurgical quality of the finished product after cutting.

(i) Effect of laser type

In laser cutting and micromachining, CO_2, Nd: YAG, fibre and ultrashort pulse lasers are the most common commercial lasers applied. These lasers are summarised in the following sub-sections.

(a) **CO_2 laser** - These lasers contain a mixture of CO_2 (laser active molecules), N_2 and He. A CO_2 laser can be operated in two modes: continuous wave (CW) and pulsed mode. The power for this laser can be within a range of few mW up to tens of kW. Different designs of CO_2 laser

available include: transverse flow (for powers greater than 4 kW, usually with a poor beam quality), fast-axial flow laser (for powers between 500 W to 8 kW, and is the most common laser for cutting applications), slow axial flow laser (for powers less than 1 kW), diffusion cooled slab laser (high energy efficiency, up to 30 kW), and sealed-off laser (for powers less than 1 kW) [69], [95], [105].

(b) **Nd: YAG laser** – The term YAG laser is usually used for solid-state lasers. YAG is the acronym for yttrium aluminum garnet (Y3Al5O12), a synthetic crystal material which became popular in the form of laser crystals in the 1960s [69], [106]. YAG lasers when doped with neodymium are known as Nd: YAG lasers. The most common Nd: YAG emission wavelength is 1064 nm. This laser can be used either in the continuous wave (CW) mode or pulsed mode [107]. Some of the noticeable characteristics of the pulsed Nd: YAG lasers are short wavelength, good focusability, and high peak power. Shorter wavelength (1.06μm) of the Nd: YAG laser ensures the high absorption of laser energy whereas very high peak powers facilitate the cutting of thick metals. Laser cutting with pulsed Nd: YAG lasers is often useful for the precision cutting applications where narrow kerf widths, small HAZ, and intricate cut profiles are desired [95].

(c) **Fibre laser** - A fibre laser is a laser in which the active gain medium is an optical fiber doped with rare-earth elements such as erbium, ytterbium, etc. The wavelength generated by a fibre laser is within the range of 1060 to 1085 nm. The fibre lasers can be excited by two methods, end-pumped and multi-mode pumped [108], [109]. The first reason a fibre laser is useful is because it is stable. When we want to deliver a laser beam, we usually need an optical fibre to move it around safely. The fibre laser generates the beam inside the fibre, so the delivery of

the beam doesn't require any complicated or sensitive optics. This makes it very stable and easy to use. The second reason a fibre laser is useful is because the beam quality is so high. The beam is generated and confined inside the small core of the fibre which means that the beam is very straight, and that it can be focused on a very small dot. The smaller the dot, the more effective the laser will be for cutting [110]. Fibre lasers have been found favourable in stent cutting after the traditional solid-state laser (Nd: YAG).

(d) **Ultrashort pulse lasers** - An ultrashort pulse laser is a laser that emits ultrashort pulses of light, generally of the order of femtoseconds to ten picoseconds. Common current ultrashort pulse laser technologies include Ti-sapphire lasers and dye lasers. These lasers have potential to process stents and other sensitive materials with minimum thermal effects and high accuracy [111], [112].

(ii) Effect of laser power

Laser power determines the direct energy going into the cutting process. Lasers are rated by their power output in terms of Watts. Cutting quality and performance are dependent on the laser power. An optimum combination of laser power and cutting speed gives the ultimate performance [113]. Determination of the required laser power needs to be done carefully as very high laser power sometimes leads to a wider kerf and excessive heat affected zone whereas very low power might result in dross due to incomplete melting [114].

(iii) Effect of Coaxial Gas Type

Generally, compressed air (used primarily for organic materials) or inert gas (e.g., nitrogen, argon, and helium) is used to exhaust melted and evaporated material from the cut zone while minimizing any excess burning. Cutting with an inert gas provides a clean cut and no oxidation as the energy

is solely from the laser beam and the assist is only used for ejecting the molten metals. High pressure inert gas (up to 14 bar) is used during the cutting process to enhance drag forces and achieve high cut quality [69], [115]. The distance between the material and nozzle through which coaxial gas is supplied is also crucial. This distance (also known as stand-off distance) must be maintained very accurately during cutting because ejection pressure varies significantly with small changes in stand-off, thereby affecting cut quality.

(iv) Effect of cutting speed

The cutting speed governs the interaction time between the laser beam and the material. Steen [69] and Decker et al. [102] suggested that there is an optimum range of cutting speeds for a given material, thickness, and beam power. In the optimum range, a thermal power balance is maintained between the exothermic burning and laser resulting in a parallel sided kerf and relatively smooth surface [116]. The cutting speed has great significance in terms of improving productivity. The kerf width and size of the heat affected zone (HAZ) decrease with increasing cutting speed [117] but if the speed is too fast, an incomplete cut will result. This is because of the short interaction time between the laser and the material. If the speed is too low, the kerf width, dross, recast and HAZ increase. In practice, cutting speeds are set below the maximum possible cut speed. This allows for a reliable process which is more tolerant of variation or fluctuation in the cut parameters (i.e. power, focus position, material thickness, assist gas flow, cutting speed).

2.3.3 Characteristics of laser cut materials

The various geometric and metallurgical quality factors sought in laser cutting include sharp corners at entry, narrow cut width, parallel sides, smooth cut surfaces, minimal thermal damage, and nonadherent dross. Due to the dynamic nature of the laser-cutting process, accurate prediction

of cutting quality becomes difficult and can be assessed by its several characteristics including kerf width, heat affected zone (HAZ), striations, dross and recast [95].

(i) Kerf Width

Kerf width is defined as the width of the cut produced during a cutting process at the upper edge of cut or with existing melting of top edge immediately below, as caused by the cutting jet. A narrow kerf width is desirable during cutting as this indicates a precise material removal process [99]. Variables such as cutting speed, laser power and coaxial assist gas jet are highly influential on the size of the kerf width [118]. The kerf width must be compensated for when designing and programming a cutting pattern.

(ii) Heat Affected Zone (HAZ)

Laser cutting is often associated with thermal effects at the surface of the cutting kerf resulting in alteration of microstructure and/or mechanical properties. This results in the formation of distinct heat-affected zone (HAZ) at the surface of the cutting edge. HAZ is often associated with undesirable effects such as surface cracking, embrittlement, decrease in weldability, decrease in corrosion, fatigue resistance, etc. Hence laser-cutting parameters are selected so as to minimize the HAZ [95]. Generally, the faster the cutting speed, the smaller the heat affected zone. This is due to reduced transfer of heat to matrix at higher cutting speeds.

(iii) Striations

Laser cutting is characterized by the formation of periodic striations along the cut edge. The presence of striations is undesirable as they may act as stress raisers causing uneven surface roughness and necessitating the further finishing operations to achieve the smooth surface [96]. Some of the causes for the formation of striations are temperature fluctuations during the process

[103], sideways burnings [119],etc. Striation-free cuts can be obtained by a proper selection of process parameters.

(iv) Dross and Recast

In most cases, laser cutting is successful in completely removing material from the kerf, however in some cases, a deposit of material slag (referred to as dross) can appear along the backside of the cut. The formation of this slag is a function of the viscosity and oxidation resistance of the molten material that was not able to be removed by the assist gas. In simpler words, dross is related with the incomplete expulsion of the melt from the bottom of the kerf [95]. Laser cutting with an inert gas jet increases the chances of dross occurrence compared to laser cutting with reactive gas. This is because the surface tension of pure metals is higher than oxidised metals. The approach to achieve dross-free cutting with an assist inert gas is by increasing its pressure up to 10 bar or more [120]. Recast is formed due to the re-deposition of the molten materials on the cut edges. This layer is usually harder and highly stressed which may lead to crack formation. Recast layer can be reduced by increasing the cutting speed where reduction of energy density on the cut area can be expected [121].

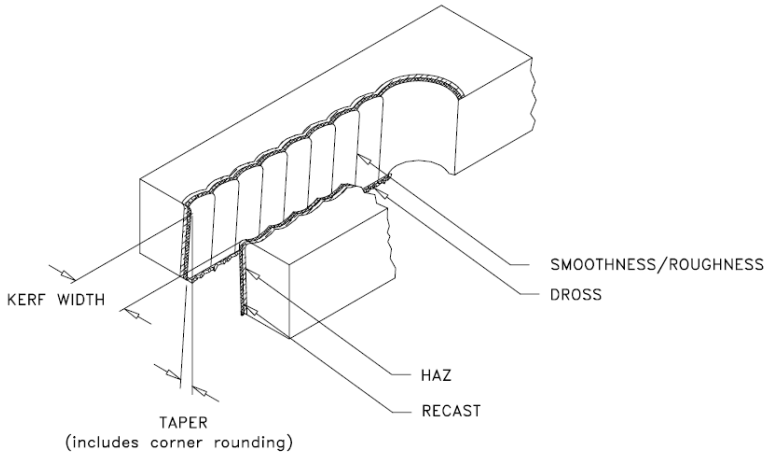

Figure 21 Schematic showing different characteristics of laser cut materials [104]

Chapter 3: Fabrication of MMM NiTi stents

Figure 22 shows the three steps, namely Laser Processing and Phase Analysis, Fabrication of MMM Stent, and Mechanical Performance Evaluation, that are performed to obtain the MMM NiTi stent developed in this study. This chapter provides a discussion on the first two steps.

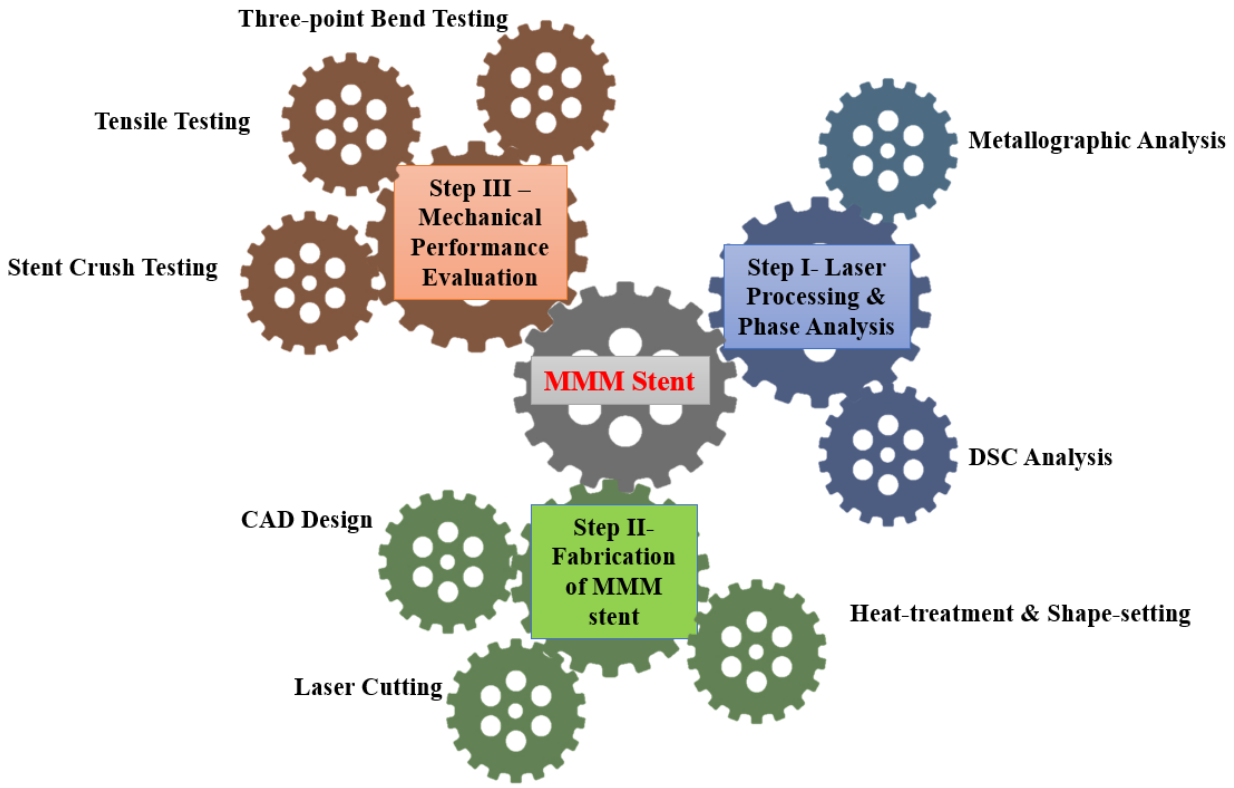

Figure 22 Steps performed to obtain MMM NiTi Stent

3.1 Laser Processing

3.1.1 Materials

Nitinol was received in the form of tubes from SAES Memry Corporation (Menlo Park, CA, USA) with an Outer Diameter: 4.000mm +/- 0.038mm and Inner Diameter: 3.400 +/- 0.05mm. These tubes were hot rolled, straightened and centreless ground. The nominal composition for the as-received NiTi tubes (referred to as BM) was 55.9 wt.% (50.8 at. %) Ni and 44.1 wt.% (49.2 at. %) Ti. The tubes were cleaned with acetone, ethanol, and deionized water prior to laser processing to remove surface contaminants.

3.1.2 Laser processing equipment and parameters

For all the mechanical and analytical experiments, laser processing of the as-received tube was conducted with an LW50 A Miyachi Unitek pulsed Nd: YAG (neodymium-doped yttrium garnet) laser source equipped with a nominal post-optical spot size of 400 µm. The tube was secured in a clamping clutch fixture to facilitate uniform heat distribution and prevent movement during rotation and processing as illustrated in Figure 23. Argon shielding gas with a flow rate of 0.71 $m^3\ h^{-1}$ (25 $ft^3\ h^{-1}$) was found to be sufficient to avoid oxidation during processing. A 300 µs pulse profile having a 200 µs down-slope (Figure 24) was used.

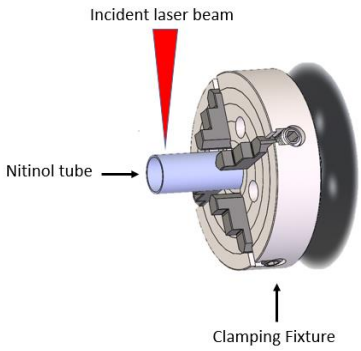

Figure 23 Laser fixture for processing NiTi tube. Laser irradiation takes place on the tube in an argon atmosphere

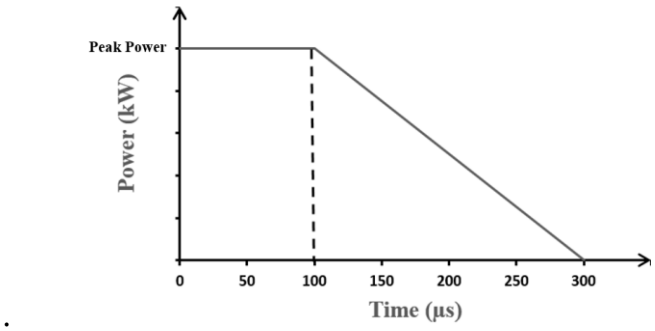

Figure 24 Laser processing schedule for processing NiTi tubes

To demonstrate the precise control of the pseudoelastic properties, the experimental samples were processed with single laser pulses and varying peak powers. These parameters were chosen to ensure only partial processing of the tube occurred. Each spot was directly adjacent to the previous spot, i.e., 0% overlap in the x-direction whereas there was a 50% overlap in the y-direction, as shown in the SEM image in Figure 25. The overlap ensures an optimum surface finish while eliminating a brittle terminal solidification. This study aims at using two different laser powers, one that is a low power and has a very shallow depth of penetration into the tube and the other that is a relatively higher power thus has more depth of penetration, to compare the mechanical properties with the change in laser power and depth of penetration of these parameters.

This comparison can provide a deeper insight into the mechanical performance of laser processed zones and its effect on the pseudoelasticity of the stents.

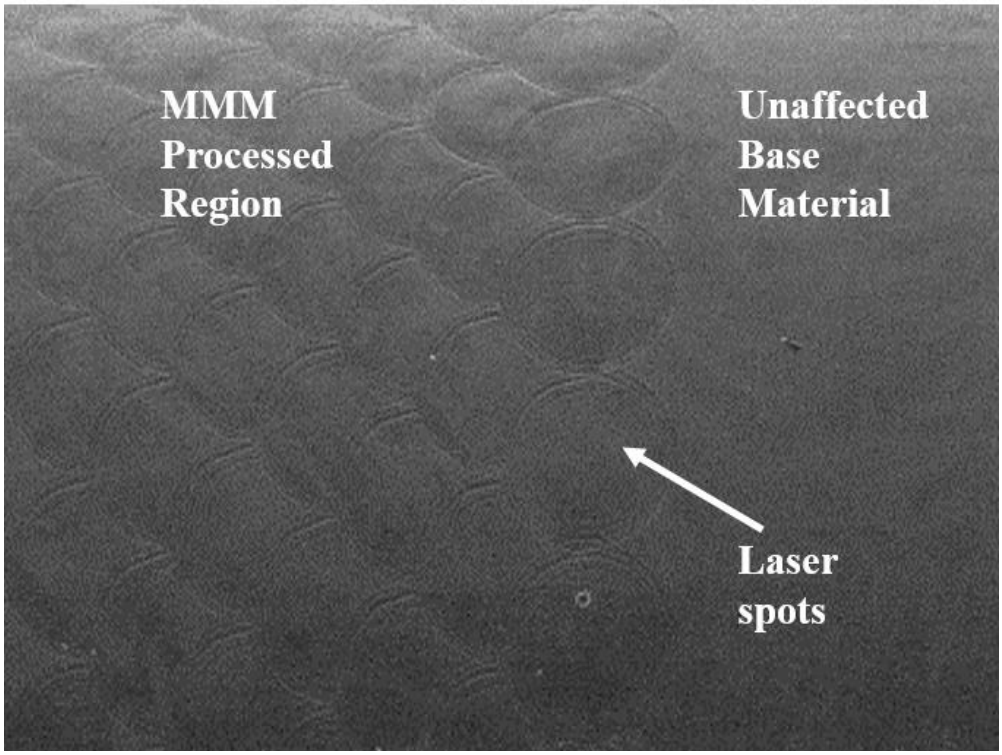

Figure 25 Top view SEM image of the Laser Processed Region

Measurements of sample cross-sections were conducted for all conditions to determine the depths of penetration. The microscopy samples were mounted in epoxy. They were ground and polished to a mirror surface with a final polish of colloidal silica. Etching time varied from 25 – 30 seconds for the samples. Etching was performed with Kroll's reagent having a composition of 2 vol% Hydrofluoric acid, 6 vol% Nitric acid and balance Distilled water. An Olympus BX51M optical microscope system with an attached camera (Q-Color 3™) was used for optical microscopy of the coarse microstructures. Through ImageJ v1.46r (open source image analysis program by National Institute of Health, USA), the depth of penetration was determined. Figure 26 provides some typical cross-sectional profile images showing the microstructure of the laser processed region.

Table 2 provides the laser powers used for processing and their depth of penetration into the tube respectively obtained from the metallographic images shown in Figure 26.

Table 2 Parameters for the laser Processed regions

Peak Power (kW)	No. of pulses	Total time (µs)	Depth of penetration (%)
0.5	1	300	**9.68 ≈ 10**
1.3	1	300	**25.54 ≈ 25**

The volume and shape of the laser processed region are dependent on the power input and energy density of the laser beam as well as the surface absorptivity and thermal conductivity of the material. This current study limits the process variable to only the input power density, keeping constant pulse time of 300 µs and pulse frequency of 1 Hz. It can be observed that the volume of the processed region increases with increasing laser power.

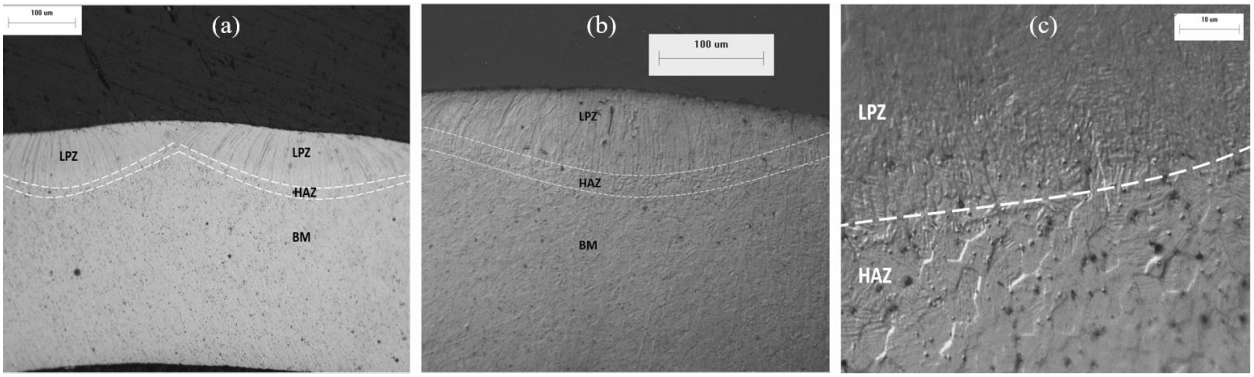

Figure 26 (a) depicts the cross-sectional view LPZ-HAZ-BM at 20x magnification, created by the low power (0.5kW) parameter used. This image shows two different spots that have been slightly overlapped in the x-direction (b) depicts the cross-sectional view LPZ-HAZ-BM at 10x magnification, created by the high power (1.3kW) parameter used (c) depicts a close-up micrograph of the LPZ and HAZ boundary at 100x magnification for the high power(1.3kW) parameter, where the recrystallized HAZ grains can be observed.

A close-up micrograph is shown in Figure 26 (a) of the boundary of the LPZ, heat affected zone (HAZ), and the BM. The equiaxed grain structure of the HAZ (also shown in (c)), and the dendritic grains of the LPZ (also shown in (a and b)) can be identified. Due to a small area of laser pulse and high undercooling at the interface of BM and molten pool, it is suspected that a high rate of solidification caused the HAZ to be relatively small in the low power parameter used. The LPZ grains can be observed solidifying epitaxially from the parent grain at the HAZ-LPZ interface in Figure 26(b).

3.2 Phase Analysis

Phase transformation curves were analyzed by differential scanning calorimetry (DSC), according to modified ASTM F2004-05 testing standard, using a thermal analysis Q 2000 system equipped (TA Instruments, New Castle, DE) with a refrigerated cooling system. Tests were conducted between -70 °C and 120 °C, controlled at a rate of 5 °C per minute. As-received and laser-processed samples were analyzed. The Thermal Analysis universal 2000 software was used to identify the austenite (A), martensite (M) start and finishing temperatures, (A_s, A_f, M_s, M_f respectively). Phase transformation information is essential as it can be used to predict shape memory and pseudoelastic behaviour of NiTi at various temperatures. These temperatures can be affected by precipitates and dislocations induced by thermomechanical processing.

DSC scans of the as-received and heat-treated BM and laser processed specimens are shown in Figure 27 (a) and (b). The stents were heat-treated after laser cutting to shape set them to a larger outer diameter. Further discussion of shape setting is done in Section 3.4 – Heat Treatment & Shape-Setting.

In binary NiTi alloys, the austenite to R-phase heating/cooling transformation hysteresis is small as per [122]. Also, it is common to have a large hysteresis for the B2 austenite to B19' martensite transformation. From the DSC result shown in Figure 27 (a), it can be seen that the martensite transformation of the BM is supressed and is not visible because it is located at a temperature lower than the DSC temperature range [123]. The R-phase transformation is caused because of high internal stresses due to the formation of Ti_3Ni_4 precipitates [122], [124], [125]. The NiTi alloy is in the B2 austenite phase below body temperature (i.e. 37 °C), so it will exhibit pseudoelastic properties. For the heat-treated BM, the R-phase/austenite transformation peaks were narrowed. Additionally, the martensite/R-phase transformation is shifted higher. This is a result of the removal of internal stresses and dissolution of the Ni intermetallics during the heat treatment process [57]. In the laser processed DSC curves, additional transformation peaks were also observed in the heating (Figure 27 (a)) and cooling (Figure 27 (b)) curves. These additional peaks are an indication of the laser processing of the material. LPZ's are indicated by black filled triangles and HAZ's are indicated by white filled triangles. It can be observed from Figure 27 (a) that there is a slight increase in the intensity of LPZ peak when there is an increase in laser power. This is due to the increase in the volume of the LPZ as was observed in Figure 26. The change in the transformation temperatures for laser processed samples can be attributed to a compositional change due to vaporization of Ni [126] and/or the dissolution of Ni-rich precipitates [127]. Table 3 shows the peak temperatures for the given DSC plots.

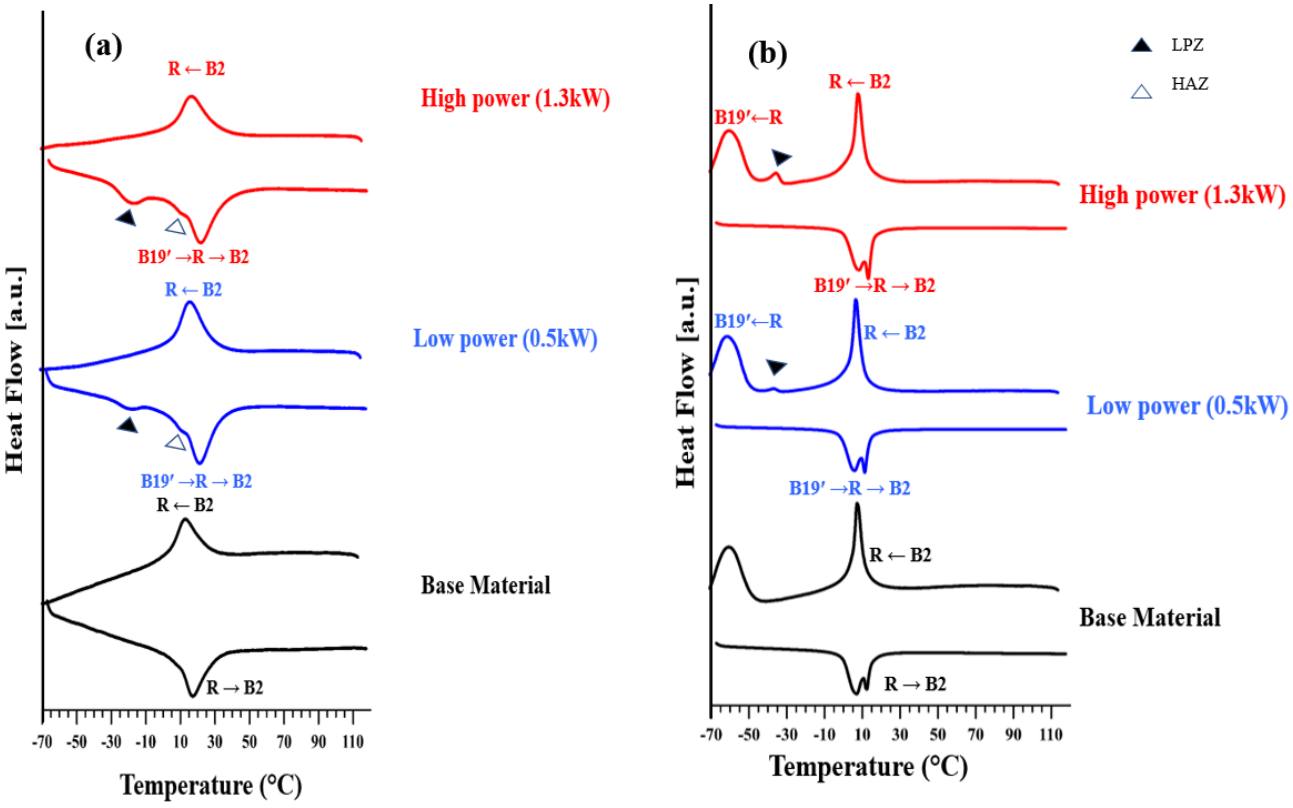

Figure 27 DSC curves for as-received BM and laser processed specimens (a) before heat treatment (b) after heat treatment at 530C for 30 mins

Table 3 Peak temperatures for BM, LP samples identified from the data obtained in Figure 27

Before Heat – treatment (°C)					**After Heat – treatment (°C)**				
	Heating			**Cooling**	**Heating**		**Cooling**		
	Austenite	HAZ	LPZ	R-phase	R-phase	Austenite	R-phase	LPZ	Martensite
BM	17.00	N/A	N/A	12.75	6.21	12.42	7.91	N/A	-60.27
Low power	21.76	9.01	-20.48	15.62	6.02	11.33	6.51	-36.72	-60.91
High power	22.26	9.46	-18.69	16.50	8.11	13.29	7.62	-35.68	-60.30

3.3 Laser Cutting

A stent laser cutting machine requires one rotation and 2 linear axes. Usually, prior to cutting, a computer aided design (CAD) data of the stent with the desired configuration is generated. The CAD data is then converted into an NC file format [128]. Finally, the data is fed to the laser cutting system and then cutting of the desired pattern can be performed with the computer numerical control (CNC) programming.

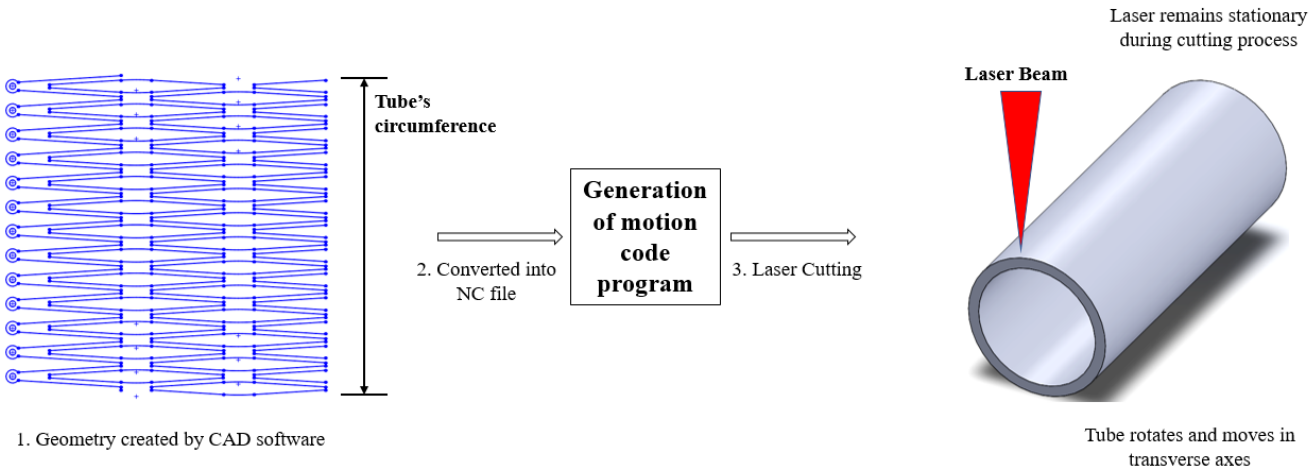

Figure 28 Schematic diagram of laser tube cutting steps

3.3.1 CAD Design

The desired pattern for a stent is developed in a two-dimensional planar form, wherein the vertical height of the unwrapped stent is equivalent to the circumference of the tube on which it will be cut. The motion controller that reads the machine code will transform the vertical coordinates to rotational coordinates to fabricate the stent. While the two-dimensional planar representation is essential for fabrication, a three-dimensional cylindrical representation is helpful for visualizing the actual stent. The stent described in this study was designed with SolidWorks Professional 2014

(Dassault Systems SolidWorks Corporation, Concord, MA). SolidWorks is a commercial CAD software package that is commonly used in the medical device industry. The following discussion provides systematic details describing the stent geometry.

A stent must be able to transform from a small diameter during insertion and delivery to the final shape-set diameter at the implantation site. If the stent is designed at its minimum diameter (as was the case for this study), it must be fabricated such that it expands to the maximum intended diameter providing the required strength, flexibility, and durability. The struts are created such that they can reliably transform from the crimped to expanded state without breaking. The variables defined in Table 4 and displayed in Figure 29, are the key aspects of the stent geometry. Note that the variable values are the values obtained for the stent geometry after expansion to the desired diameter. Figure 30 (a) shows a 3D CAD model of a laser cut stent and an expanded stent and (b) shows a fully wrapped stent model showing the design used for this study.

Table 4 Variables used in the stent geometry

Denotation	**Value**	**Definition**
N_{col}	13	Number of columns of struts along the length of the stent
D_{tube}	4 mm	Outer diameter of the tube from which the stent is fabricated
t_{raw}	0.3 mm	Wall thickness of the tube from which the stent is fabricated
w_{strut}	0.183 mm	Strut width
L_{strut_inner}	2.86 mm	Length of a strut between the quadrants of the inner arcs of opposite apices
w_{apex}	0.48 mm	Width of an apex
$X_{connector}$	1.21 mm	Axial gap between adjacent columns of struts
D_{set}	8.6 mm	Expanded diameter of the stent after shape-setting

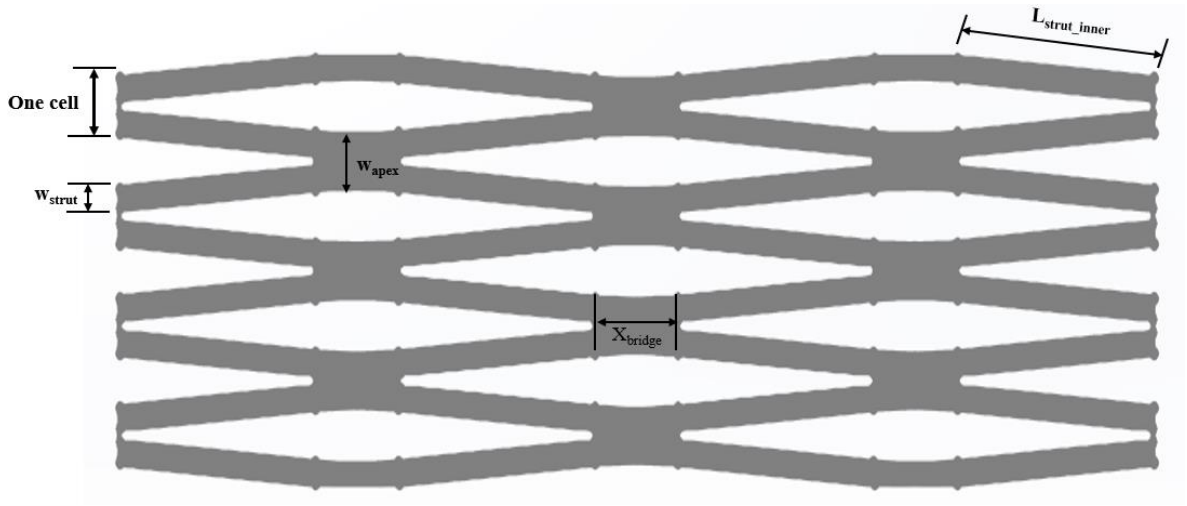

Figure 29 Schematic showing different variables in a stent geometry

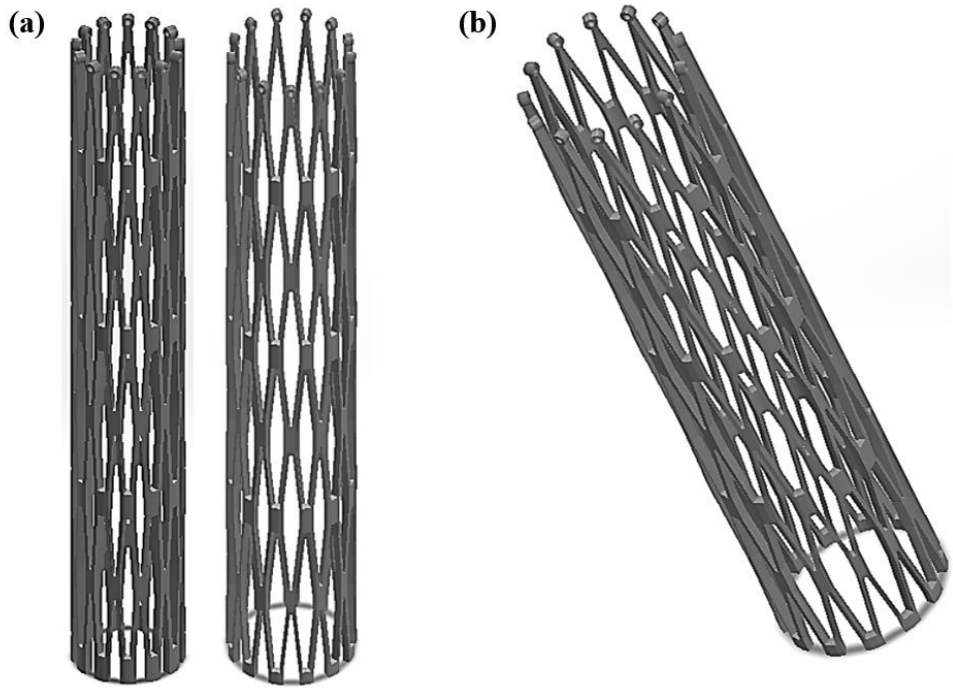

Figure 30 (a) 3-D CAD model of a laser cut stent (left), expanded stent (right) (b) 3-D wrapped geometry showing the intricate design for the MMM stent

3.3.2 Cutting

All experiments involving laser micromachining were carried out using a pulsed Rofin Starcut© Tube Nd: YAG laser. The tube sample was loaded into the workstation horizontally and was guided by a bushing mechanism. During the cutting process, the NiTi tube was rotated and moved in the transverse axes directed by the motion code movement while the laser remained stationary. Preliminary experiments were carried out to determine the appropriate processing parameters to be used for further investigation. This preliminary investigation was done by taking literature from Kathuria [129]–[131], Raval et. al [132] and Meszlenyi et. al [133] as a basis. The chosen average power, cutting speed and repetition rate were based on the sufficient energy needed to cut nitinol. The laser and process specifications for micromachining are listed in Table 5. These parameters are specific to the tube dimensions: Outer Diameter: 4mm Inner Diameter: 3.4mm. Any change in dimensions will require tuning of the parameters.

Table 5 Process Parameters for machining NiTi

Process Parameters	**Unit**	**Values**
Pulse width	ms	0.23
Pulse frequency	Hz	150
Voltage	V	600
Cutting speed	mm/s	1.5 – 2
Assist Gas		Ar
Gas Pressure	bar	12
Nozzle Stand – off	mm	0.55
Focal spot size	µm	35
Pierce Delay	sec	0.5

A narrow and consistent kerf width is required to allow some space for electropolishing, which involves material removal that causes strut width reduction. It is important to maintain the kerf width because the intricacy of the cutting pattern is required for uniform stent expansion. The kerf width measured in this study is 40 μm. Excessive heat from the laser beam causes thermal effect to the stent material resulting in embrittlement and undesirable heat affected zones adjacent to the laser cut. This deficiency can cause stent rupture when the stent is expanding during implantation [134]. The use of a high gas pressure (12 bar in this case) can reduce the heat affected zone. Also, the HAZ is detected with the help of DSC measurements and hence it can be used as a technique to see if the process parameters are contributing towards the HAZ or not.

3.4 Heat Treatment (HT) and Shape-Setting

Shape setting is the process by which the final, specified shape of the metal is configured and programmed. Shape setting nitinol can be done in many ways but the basic method remains constant: design and build a custom fixture, secure nitinol to the fixture, heat treat to the required temperature, cool, and remove nitinol. For this study, a steel rod was used for shape-setting. A steel rod with an outer diameter of 8 mm was inserted inside the laser cut stent (Figure 31(c)). This effect deformed the stent to its maximum operating size without any signs of cracking or mechanical failure. To maintain the shape, the laser cut stents were shape-set by heat-treating at 530°C in a pre-heated Thermo Electron Corporation Lindberg/Blue M furnace for 30 minutes. Subsequently, they were quenched in cold water to avoid formation of Ni_3Ti [135]. After shape setting, the final OD of the fully expanded stent was 8.6 mm (Figure 31 (b)). Heat treatment is not only capable of making the nitinol stents retain the preferred shape, but it also controls the

transformation temperatures, which determines the superelastic performance at body temperature [136].

A salt bath with 60% sodium nitrate and 40% potassium nitrate content is used for immersion of the nitinol stents during the heat treatment. Molten salt baths act as heat sinks which allows the metal to absorb the heat such that the temperature at the centre and the surface of the piece, increase at relatively the same rate, therefore heating in molten salts is very uniform. Parts immersed in a molten salt bath during heat treatment cycles are protected from the atmosphere and the damaging oxide scale formation caused by water vapor, oxygen, and carbon dioxide, found in most furnaces, is eliminated. When a part is heat-treated in a salt bath, it develops a thin cocoon of solidified salt. This cocoon protects the part from rapid initial heating and resulting thermal shock. As the cocoon eventually melts, the part is uniformly heated, minimizing any distortion and preventing cracking [137].

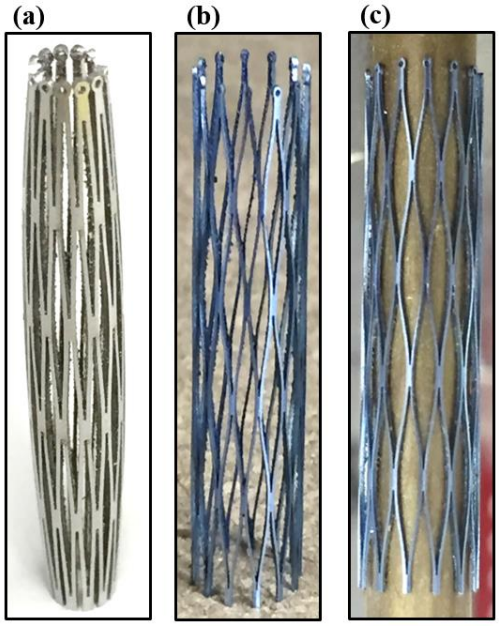

Figure 31 (a) Laser cut stent having an OD of 4 mm (b) expanded stent with an OD of 8.6 mm (c) laser cut stent secured to a steel rod of 8 mm diameter

3.5 Chapter Summary

This chapter discusses the different laser parameters used for this study. Differential Scanning Calorimetry analysis shows an increase in the volume of martensite formed upon increasing the laser power. The change in transformation temperatures was possibly due to vaporization of Ni or dissolution of Ni-rich precipitates. Laser cutting showed that a short pulse width/duration, small focal spot size, low power, moderate nozzle stand-off distance, moderate cutting speed and a low frequency are required for precise material removal and a narrow kerf width. A heat-treatment of 530°C for 30 minutes was successful for shape-setting the stent to 8.6 mm OD while maintaining the pseudoelastic properties.

Chapter 4: Evaluation of the mechanical performance of MMM NiTi stents

The association of in-stent restenosis and reocclusion with stent fractures has led to an increase of interest in the mechanical properties of NiTi stents [138]. A proper understanding of the biomechanical forces at the stent implantation site are required to avoid the cases of stent fractures and failures [139]. When a BM stent is laser processed continuously across the length, a change is expected in the bulk mechanical performance of the stent. Since the LPZ's are non-pseudoelastic zones [127], it is observed that the increase in volume of these zones causes the proportionate decrease of the pseudoelastic response of the stent. To better control the PE modification, this chapter discusses the effect of processing parameters on the mechanical properties. Each test was performed in triplicate using three separate specimens. All the specimens used for the three-point bend tests, crush tests and tensile tests were heat-treated at 530°C for 30 mins.

4.1 Three-Point Bend Testing

It is important to know the mechanical performance of a stent when placed under a constant bending force. Bending stiffness can be determined from a three-point bend test for stent coupons. Some work done by Pelton et.al. [140] used a similar diamond design and carried out some FEA analysis on just the quarter symmetry of the stent and found results that agreed with their experimental force-displacement results. Hence, coupons were used for this test and results can be extrapolated to that of a full strut. The specimens used were rectangular coupons and their dimensions were 30 mm (length) x 0.183 mm (width) x 0.3 mm (thickness). The width of the

coupon was kept as 0.183 mm since the strut width is 0.183 mm and the bending performance needs to be translated to the bending of the struts in the stent. These tests were carried out in a bio-bath maintained at 37°C temperature, the specified operating temperature, for all tests. The test setup is shown in Figure 32. The crosshead rate was set to 2.5 mm/min. These coupons are rested between supports which were spaced 10 mm apart and loaded using a 0.1 mm diameter indenter and fulcrum as shown in Figure 32.

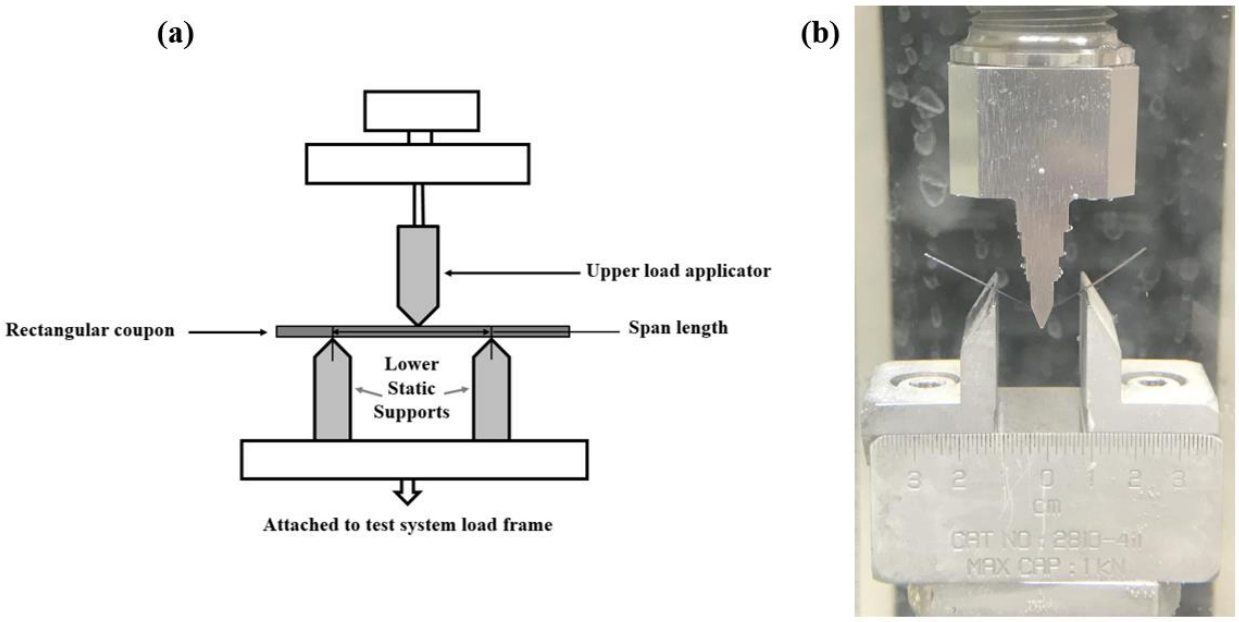

Figure 32 (a) Schematic of 3-point bending test apparatus (b) actual test setup showing bending of the coupon

As shown in Figure 33, the bending forces of laser processed coupons demonstrated a reduction with increasing laser power. Taken at 3 mm deflection, the bending forces during unloading were 0.30 N, 0.25 N, and 0.15 N for BM, low-power, and high-power specimens respectively. At the same time, the residual strain from bending increases with laser power as well, which were 0.016 mm, 0.05 mm, and 0.20 mm for BM, low-power, and high-power specimens, respectively. Although there is observable residual strain, such low residual strains should not negatively affect

the performance of the stents. Stents operate within the pseudoelastic plateau only and never experience a complete unloading of force or a complete relaxation of strain (refer to Figure 8). This helps to maintain a constant exertion force on the vessel walls. Therefore, the effect of this residual strain can be neglected because in this case it is relatively low strains. Very high-power laser conditions have not been tested to avoid excessive residual strain.

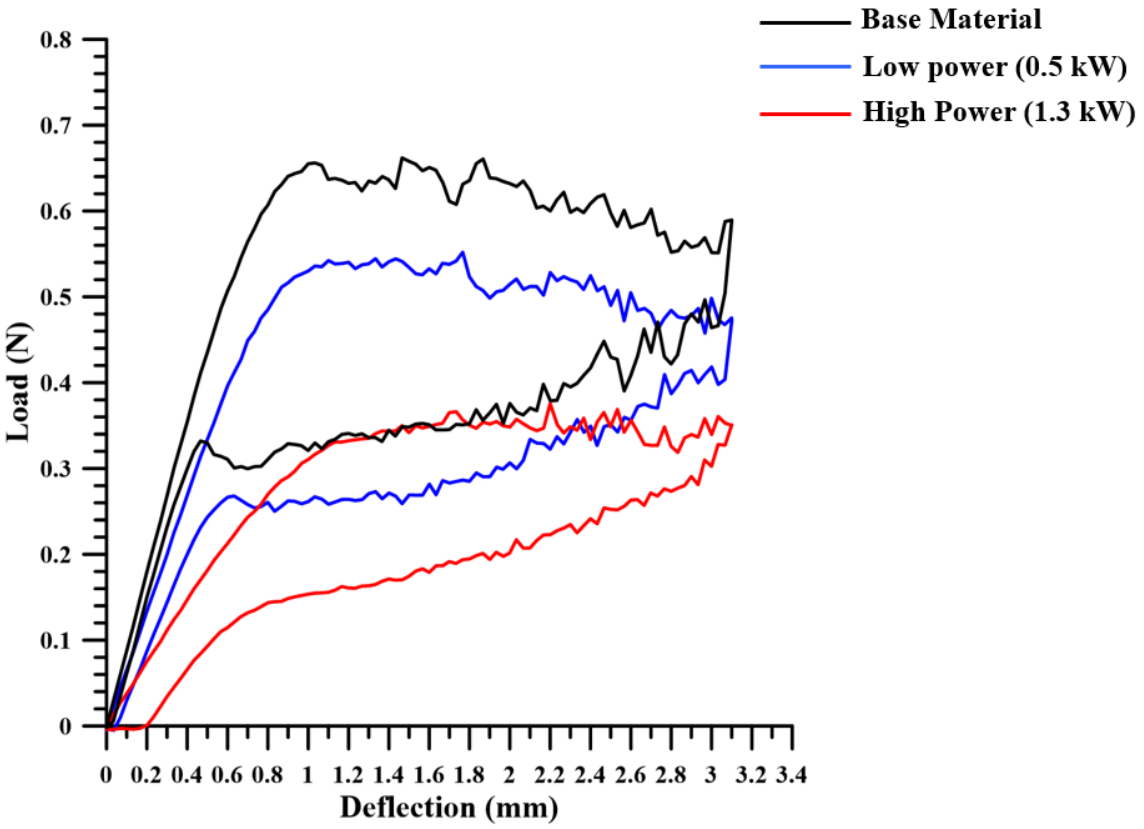

Figure 33 Three-point bending response of base metal, low-power, high-power coupons modified through laser processing

4.2 Stent Crush Testing

Crush resistance is defined as the ability of a stent to resist external pressure forces exerted on the stent and arterial walls, without plastic deformation (ISO/TS 15539). One of the main requirements

of a stent design is to provide enough radial force to maintain the opening of the artery in which it is inserted. The amount of radial force or crush resistance provided by each stent depends mainly on the stent design, geometry and material properties [141]. The design of stents with high radial force has the theoretical objective of minimizing their recoil when used in arterial walls with varying morphologies of plaque [142]. The testing apparatus used to measure radial force or crush resistance of stents is shown in Figure 34. The stent is crushed/compressed between a V-shaped (60° angle) lower gripping jaw and crushed against a T-shaped upper jaw which has a flat surface that covers the OD of the stent while crushing it. The base and the top of the device are joined to a vertical movement system which allows stress to be applied on the stent between the gripping block. All the tests are carried out at 37°C inside a bio-bath. The fully expanded stent (8.6 mm OD) is the test specimen for BM and LP stents.

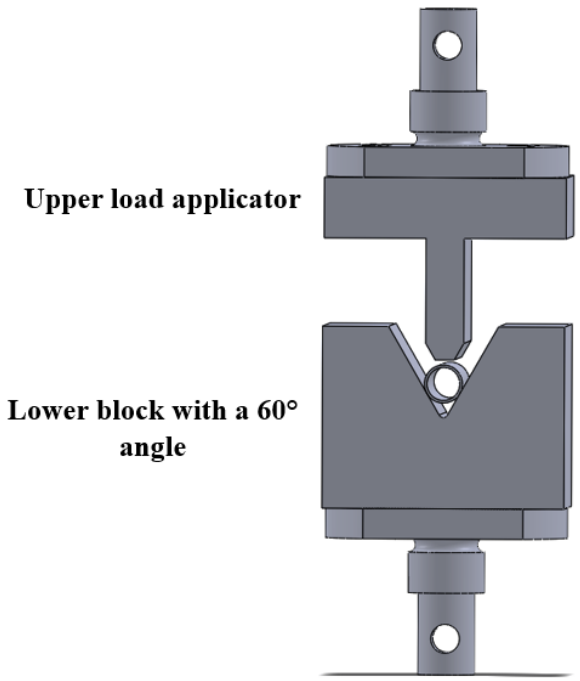

Figure 34 Schematic of the experimental setup to determine the radial strength of the stent

The stents are placed in the V and are subjected to localized stress at three points. These are the points where the stents are in contact with the base V (2 points) and the upper jaw (1 point). The local deflection is recorded each time after the stress is applied to obtain a force-deflection curve. A deflection of 4.5 mm was applied to each stent to compare the stresses obtained for different stents. The stress experienced by the stents during these experiments is due to uniformly applied pressure around the stent. As shown in Figure 35, the radial forces exhibited by the BM, low-power, and high-power stents were 7.7 N, 6.5 N, 5.4 N respectively. According to these numbers we note that the radial forces decrease with increase in laser processing powers.

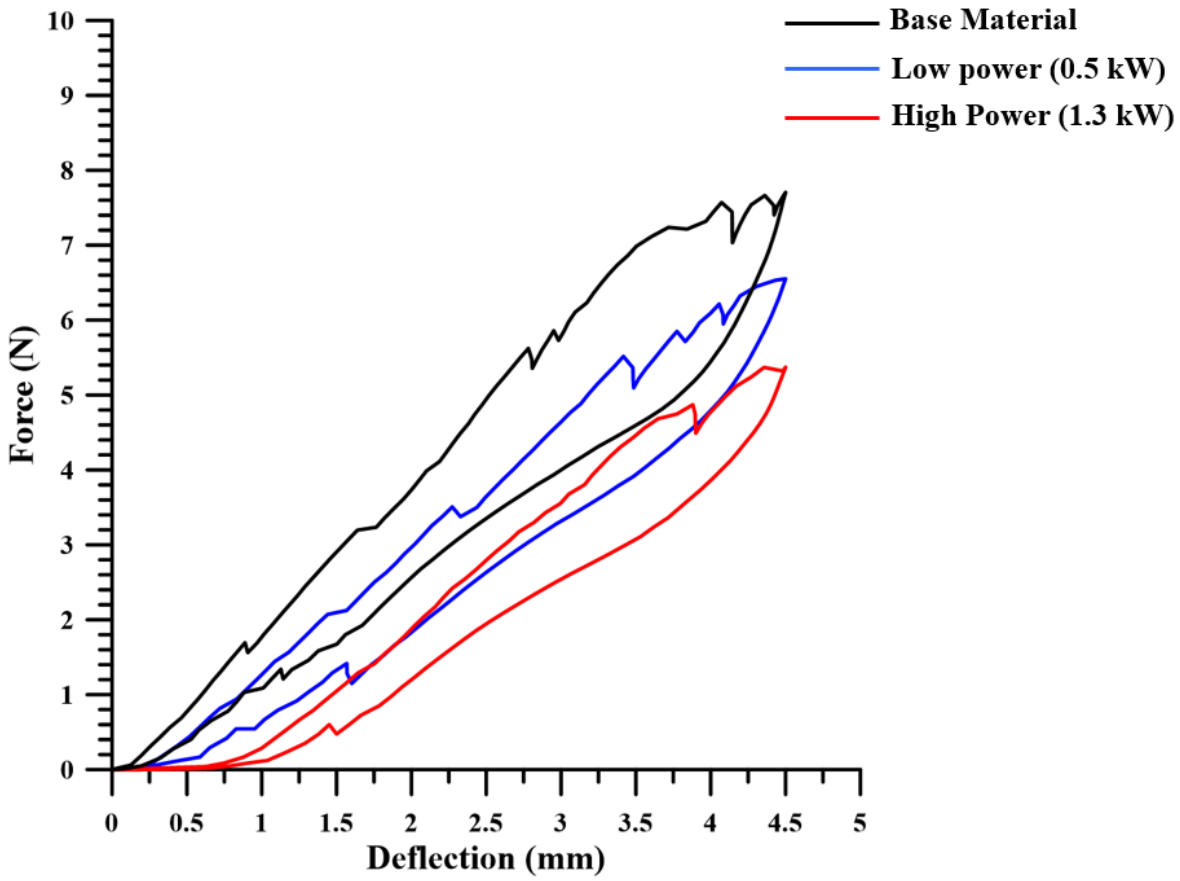

Figure 35 Crush test response of base metal, low-power, high-power stents modified through laser processing

4.3 Tensile Testing

Thermomechanical recovery of the nitinol samples was assessed using an Instron™ 5565 tensile tester with a table-top visual extensometer which was retrofitted with a temperature chamber. Tensile tests were conducted on dog-bone coupons (Figure 36 (a)) that were laser micro machined from nitinol tubes. An SEM image of the LP dog-bone coupon is also shown in Figure 36 (b). The samples were tested at body temperature (37 °C) at a rate of 0.4 mm/min to 6% strain. The gauge length for all the samples was set at 25 mm. The thickness of the sample was 0.3 mm and the width was 0.85 mm. White Styrofoam balls were glued to the sample as markers and tracked during each test. A two-part epoxy was used to stick the balls at the ends of the dog-bone coupons and ensure no slipping would occur during the test. The epoxy took about 20 minutes to cure after which the samples were tested. The test setup is illustrated in Figure 37. A camera attached to the door of the chamber was used to track the position of the Styrofoam balls during the tests (Figure 37 (c)).

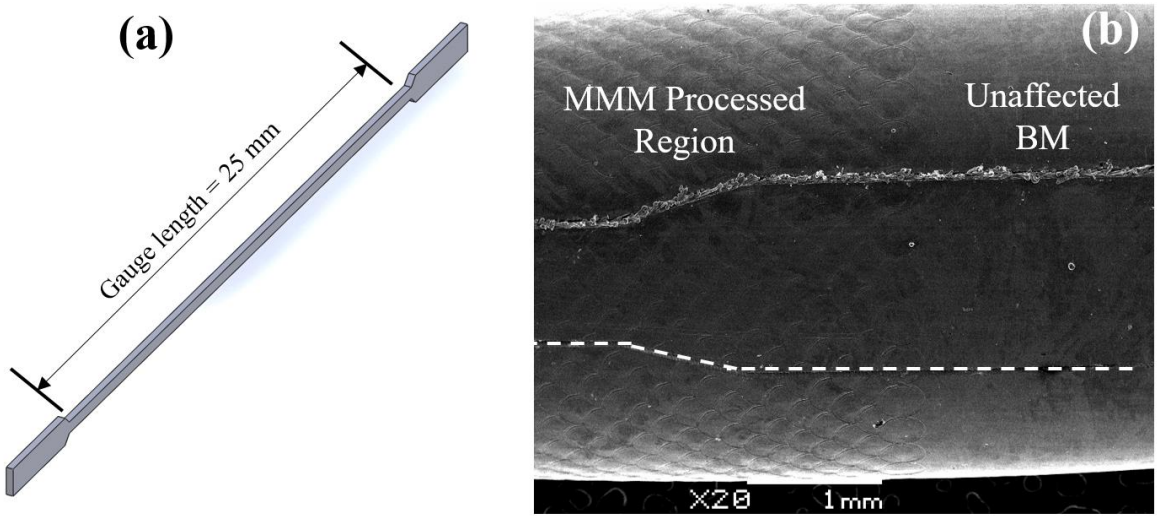

Figure 36 (a) Illustration of the laser cut dog-bone coupon (b) SEM image of a dog-bone coupon which shows the MMM Processed region alongside the BM. The coupon is shown in white dotted lines

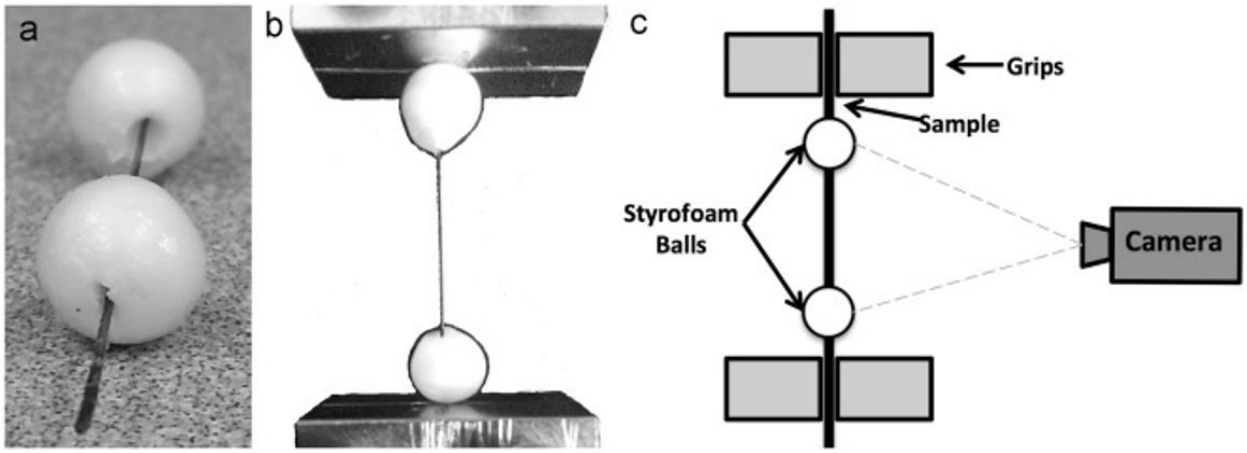

Figure 37 (a) Styrofoam balls attached to the test specimen (b) specimen loaded in grips with white balls attached (c) schematic depicting the visual extensometer setup [143]

The tensile response of the NiTi dog-bone coupon specimens are provided in Figure 38. As mentioned earlier in the chapter, that LPZs are non-PE zones, it was proposed that the increase in volume of these non-pseudoelastic zones causes the proportionate decrease of the pseudoelastic response of the wire. This means that with increase in laser power, there should be a decrease in the PE plateau stress.

BM, low- power, and high-power samples show pseudoelastic responses with an average forward pseudoelastic force of 425 MPa, 380 MPa, 335 MPa respectively and an average return pseudoelastic force of 220 MPa, 125 MPa, 85 MPa respectively (Figure 38). As we can see, the LP NiTi specimens exhibited pseudoelasticity at lower plateau stresses than the BM specimen. According to these numbers and the calculations below, we can show a correlation between the forward pseudoelastic plateau and penetration depth.

$$\text{Area of the specimen} = 0.255\ \text{mm}^2$$

$$\text{Stress} = \text{Force} / \text{Unit Area}$$

Considering the forces for,

$$BM = 425\ MPa \times 0.255\ mm^2 = 108.375\ N$$

$$\text{Low power (0.5kW) parameter} = 380\ MPa \times 0.255\ mm^2 = 96.9\ N$$

$$\text{High power (1.3kW) parameter} = 335\ MPa \times 0.255\ mm^2 = 85.425\ N$$

To find the percentage of force reduction for the LP parameters with respect to BM,

$$\text{Low power (0.5kW) parameter} = (108.375 - 96.9) / 108.375 \approx \mathbf{10\%}$$

$$\text{High power (1.3kW) parameter} = (108.375 - 85.425) / 108.375 \approx \mathbf{25\ \%}$$

These values agree with the measurements observed for the LPZ penetration depths for each of these powers (refer to Table 2). Hence **t**he difference in the forward pseudoelastic response is in accordance with the proposed correlation. According to this correlation, it can be predicted how the forward plateau stresses will be reduced with increasing penetration depth of the LPZ.

The return plateau sees a more significant drop that cannot be attributed to the LPZ area alone. This reduction maybe the result of a slightly larger grain size in the retained base material [144], [145]. It was observed by DSC (refer to Table 3) that the transformation temperature of the retained BM shifted slightly to a higher temperature, which may be an indication of a very minor annealing of the retained base material during the laser processing.

The force contributions for the forward plateau of the tensile cycle for the laser processed specimens were the plastic deformation of the LPZ through the low stress slip mechanism and phase transformation of the remnant BM from B2 austenite phase to B19' stress induced martensite phase (SIM). In the return plateau of the tensile cycle, the force contributions were the reverse phase transformation of the remnant BM from B19' to B2 and the compression of the deformed LPZ back to the original gauge length by the pseudoelastic BM [127].

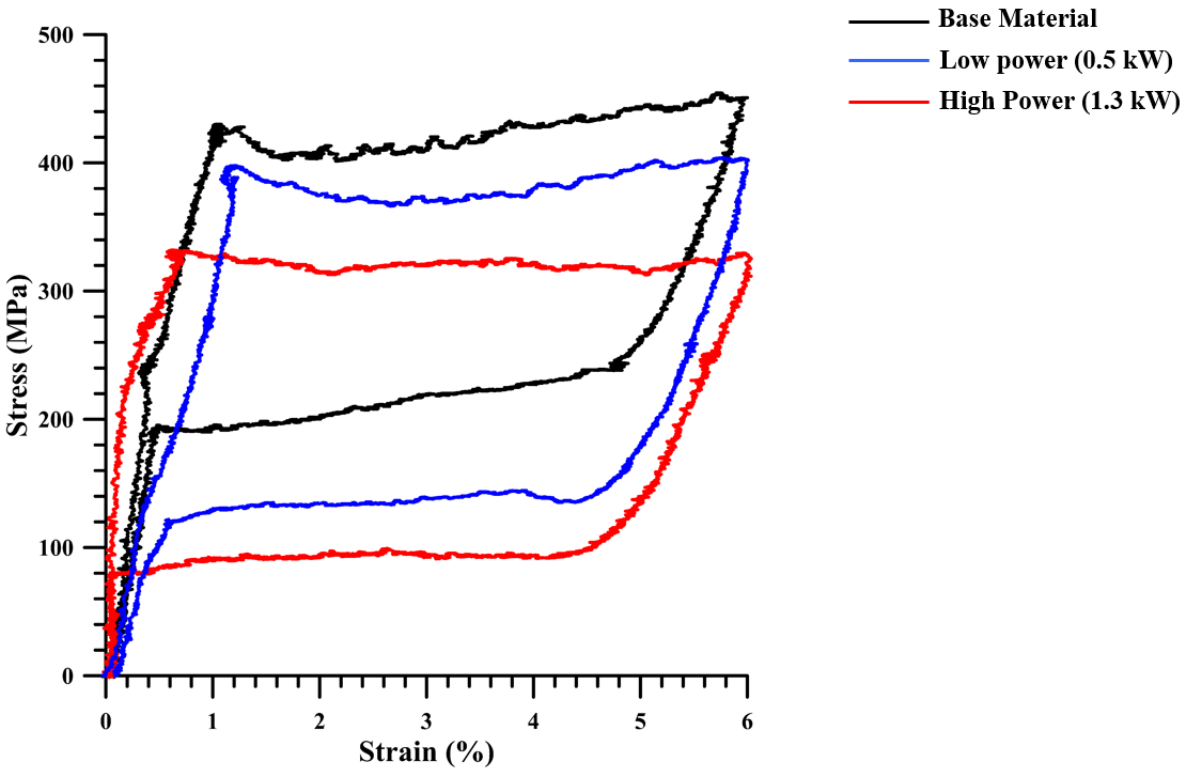

Figure 38 Pseudoelastic response for BM and LP specimens

4.4 Chapter Summary

To better control the PE modification, this chapter had set out to uncover the relationship that exists between the laser processing parameters and the mechanical properties exhibited by these as compared to BM. A trend is seen in the results obtained from the three-point bend tests, stent crush tests and tensile tests. We observe that the pseudoelastic force decreases with an increase in the laser power. The mechanism behind the pseudoelastic force modification is the effect of the replacement of a portion of the BM by a series of LPZs. This study has opened the capability for precise control over the PE property of a stent and the author has been successfully able to fabricate a stent that has 2 different regions: BM and LP region in the same stent. Hence a variable radial force can be achieved and this capability for precise control over the pseudoelastic property of

SMA materials shall offer excellent improvements to the design freedom and the functionality of stents.

Chapter 5: Conclusions & Future Work

5.1 Conclusions

1. Laser processing has enabled the fabrication of a stent that has two unique thermomechanical responses. A stent having two different regions: LP and BM side by side has been obtained in this work. To the author's knowledge, this study is the first example of a NiTi MMM stent that can have two different PE zones as the result of localized laser processing.
2. Upon increasing the laser power, the depth of laser penetration in the NiTi tube increases. The volume of HAZ also increases with an increase in laser power. The DSC analysis confirms this.
3. The laser power was shown to strongly influence the mechanical properties (tensile strength and crush resistance) of the laser processed Nitinol stent. By increasing laser power and subsequently increasing the laser processed zones, pseudoelastic stress can be decreased.
4. Laser processing technology has demonstrated the capability of achieving variable forces across the length of a stent by locally altering phase transformation dynamics within processed material domains. Through laser processing, NiTi SMAs can be exploited to unlock additional thermomechanical characteristics.

5.2 Future Work

1. This study adds only two different PE zones. Adding additional zones in the future can also help in having variable forces across the length of the stent in case of multiple uneven healthy and unhealthy regions in the arterial walls.
2. Particle-induced X-ray emission analysis is strongly suggested to gain accurate compositional analysis. Another method for compositional analysis is the Energy Dispersive X-ray spectroscopy (EDX). EDX can be easily found and is also a cost-effective technique, although, a drawback of this technique is that analytical accuracy is commonly near ± 1%. In case of Ni vaporization in NiTi alloy, the change in composition is less than 1% and hence EDX will not be able to give a accurate and reliable data. Therefore, EDX measurements are not performed for this study.
3. The bending characteristic, a major design factor in medical implants, has not been fully considered when studying the cardiovascular stent's mechanical properties. The effect of dynamic bending might have a significant impact on the stent's stress distribution, fatigue performance and overall stress on the vessel, and hence the bending characteristics need to be studied and analysed.
4. Finite element analysis (FEA) can be used for the simulation of expansion of the stent in the artery. It can help in determining the maximum expansion stress in the stent due to opening of the struts when the stent opens to the final Outer Diameter.
5. The use of stents in the human body requires zero failure since the human life is at risk. Fatigue life testing should be carried out at the macroscopic and microstructural level since the fatigue life of nitinol is highly dependent on the stress concentrations in localized

martensitic transformations, occurring either due to structural slip bands or incurred through oxygen and carbide inclusions [146]. Hence, only a macroscopic study will be inadequate in predicting the long-term fatigue life.

6. One of the limitations of this study is that the pattern of deforming forces used for stent crush tests may be different from the in vivo forces. Hence in vivo tests results will help in determining the effect of localized sharp spur of calcified plaque.
7. Analysis of the mechanical behavior of the MMM stent under artery and blood flow effect is required. This will allow to collect some clinical data that can then develop models that will match suitable stent configuration with the type of the patient diseases. Clinical performance reports along with FEA analysis can be used for simulating the real world physical situation, using refined numerical studies for stent-artery, stent-flow interactions cases. Computational modelling can also be used to quantitatively characterize the hemodynamic conditions in an idealized model of artery. It will progress the potential application of computational blood flow simulations to stent implantation.

The tailoring of medical devices to patients based on their unique needs, has started becoming achievable in this era. Recent advances in the field of biomedical devices, medical imaging and modeling have allowed the construction of patient specific artery models for the prediction of individualized stent performance. By combining patient specific results with existing knowledge of endothelial response to mechanical stimuli, stent properties can be optimized to reduce or eliminate the risk of CVD.

References

[1] Y. Ozaki, A. G. Violaris, and P. W. Serruys, "New stent technologies.," *Prog. Cardiovasc. Dis.*, vol. 39, no. 2, pp. 129–140, 1996.

[2] L. B. Tan, D. C. Webb, K. Kormi, and S. T. S. Al-Hassani, "A method for investigating the mechanical properties of intracoronary stents using finite element numerical simulation," *Int. J. Cardiol.*, vol. 78, no. 1, pp. 51–67, 2001.

[3] A. J. Carter *et al.*, "Progressive vascular remodeling and reduced neointimal formation after placement of a thermoelastic self-expanding nitinol stent in an experimental model.," *Cathet. Cardiovasc. Diagn.*, vol. 44, no. 2, pp. 193–201, Jun. 1998.

[4] E. Rechavia *et al.*, "Temporary arterial stenting: Comparison to permanent stenting and conventional balloon injury in a rabbit carotid artery model," *Cathet. Cardiovasc. Diagn.*, vol. 41, no. 1, pp. 85–92, 1997.

[5] S. Sheth, F. Litvack, V. Dev, M. C. Fishbein, J. S. Forrester, and N. Eigler, "Subacute thrombosis and vascular injury resulting from slotted-tube nitinol and stainless steel stents in a rabbit carotid artery model.," *Circulation*, vol. 94, no. 7, pp. 1733–1740, Oct. 1996.

[6] J. Ryhänen, *Biocompatibility Evaluation of Nickel- Titanium Shape Memory Metal Alloy of Nickel-Titanium Shape*, vol. 41, no. 3. 1999.

[7] B. Thierry, M. Tabrizian, C. Trepanier, O. Savadogo, and L. Yahia, "Effect of surface treatment and sterilization processes on the corrosion behavior of NiTi shape memory alloy.," *J. Biomed. Mater. Res.*, vol. 51, no. 4, pp. 685–693, Sep. 2000.

[8] B. Thierry, Y. Merhi, L. Bilodeau, C. Trépanier, and M. Tabrizian, "Nitinol versus stainless steel stents: acute thrombogenicity study in an ex vivo porcine model," *Biomaterials*, vol.

23, no. 14, pp. 2997–3005, 2002.

[9] M. Henry *et al.*, “Clinical Experience with a New Nitinol Self-Expanding Stent in Peripheral Arteries,” *J. Endovasc. Ther.*, vol. 3, no. 4, pp. 369–379, Nov. 1996.

[10] C. Rogers and E. R. Edelman, “Endovascular Stent Design Dictates Experimental Restenosis and Thrombosis,” *Circulation*, vol. 91, no. 12, pp. 2995–3001, 1995.

[11] T. Duerig, a Pelton, and D. Stöckel, “An overview of nitinol medical applications,” *Mater. Sci. Eng. A*, vol. 273–275, pp. 149–160, 1999.

[12] T. W. Duerig, D. E. Tolomeo, and M. Wholey, “An overview of superelastic stent design,” *Minim. Invasive Ther. Allied Technol.*, vol. 9, no. 3–4, pp. 235–246, 2000.

[13] K. Otsuka and X. Ren, “Physical metallurgy of Ti-Ni-based shape memory alloys,” *Prog. Mater. Sci.*, vol. 50, no. 5, pp. 511–678, 2005.

[14] W. Nitinol, A. R. Pelton, D. Stockel, and T. Duerig, “Medical Uses of Nitinol Pelton , Stoeckel , Duerig Medical Uses of Nitinol,” 2000.

[15] S. Shabalovskaya, J. Anderegg, and J. Van Humbeeck, “Critical overview of Nitinol surfaces and their modifications for medical applications,” *Acta Biomater.*, vol. 4, no. 3, pp. 447–467, May 2008.

[16] M. I. Khan, A. Pequegnat, and Y. N. Zhou, “Multiple Memory Shape Memory Alloys,” *Adv. Eng. Mater.*, vol. 15, no. 5, pp. 386–393, May 2013.

[17] E. Claes *et al.*, “Mechanical properties of human coronary arteries,” in *2010 Annual International Conference of the IEEE Engineering in Medicine and Biology*, 2010, pp. 3792–3795.

[18] D. Martin and F. Boyle, “Finite element analysis of balloon-expandable coronary stent

deployment: Influence of angioplasty balloon configuration," *Int. j. numer. method. biomed. eng.*, vol. 29, no. 11, pp. 1161–1175, Nov. 2013.

[19] D. Stoeckel, C. Bonsignore, and S. Duda, "A survey of stent designs," *Minim. Invasive Ther. Allied Technol.*, vol. 11, no. 4, pp. 137–147, Jan. 2002.

[20] Cleveland Clinic, "Heart & Blood Vessels: Your Coronary Arteries." [Online]. Available: https://my.clevelandclinic.org/health/articles/heart-blood-vessels-coronary-arteries.

[21] D. Lee Kulick, "Coronary Heart Disease Screening Tests (CAD)." [Online]. Available: http://www.medicinenet.com/coronary_artery_disease_screening_tests_cad/article.htm.

[22] D. M. Martin and F. J. Boyle, "Drug-eluting stents for coronary artery disease: A review," *Med. Eng. Phys.*, vol. 33, no. 2, pp. 148–163, Mar. 2011.

[23] E. Alegría-barrero, "Maximal expansion capacity with current DES platforms : A critical factor for stent selection in the treatment of left main bifurcations?," no. January, 2015.

[24] T. Duerig and M. Wholey, "A comparison of balloon- and self-expanding stents," *Minim. Invasive Ther. Allied Technol.*, vol. 11, no. 4, pp. 173–178, Jan. 2002.

[25] J. M. Garasic, E. R. Edelman, J. C. Squire, P. Seifert, M. S. Williams, and C. Rogers, "Stent and Artery Geometry Determine Intimal Thickening Independent of Arterial Injury," *Circulation*, vol. 101, no. 7, pp. 812–818, Feb. 2000.

[26] M. Wholey and E. Finol, "Designing the ideal stent," *Endovascular Today*, p. 25, Mar-2007.

[27] X. Ma *et al.*, "Drug-eluting stents," *Int. J. Clin. Exp. Med.*, vol. 3, no. 3, pp. 192–201, Jul. 2010.

[28] B. Peters, P. Ewert, and F. Berger, "The role of stents in the treatment of congenital heart disease: Current status and future perspectives," *Ann. Pediatr. Cardiol.*, vol. 2, no. 1, p. 3,

2009.

[29] J. Kreutzer and J. J. Rome, “Open-cell design stents in congenital heart disease: A comparison of IntraStent vs. Palmaz stents,” *Catheter. Cardiovasc. Interv.*, vol. 56, no. 3, pp. 400–409, Jul. 2002.

[30] D. R. Whittaker and M. F. Fillinger, “The Engineering of Endovascular Stent Technology: A Review,” *Vasc. Endovascular Surg.*, vol. 40, no. 2, pp. 85–94, 2006.

[31] A. García, E. Peña, and M. A. Martínez, “Influence of geometrical parameters on radial force during self-expanding stent deployment. Application for a variable radial stiffness stent,” *J. Mech. Behav. Biomed. Mater.*, vol. 10, pp. 166–175, 2012.

[32] P. Maurovich-horvat, M. Ferencik, S. Voros, B. Merkely, and U. Hoffmann, “Comprehensive plaque assessment,” *Nat. Publ. Gr.*, no. April, 2014.

[33] A. Holton, E. Walsh, A. Anayiotos, G. Pohost, and R. Venugopalan, “Comparative MRI Compatibility of 316L Stainless Steel Alloy and Nickel???Titanium Alloy Stents,” *J. Cardiovasc. Magn. Reson.*, vol. 4, no. 4, pp. 423–430, 2003.

[34] G. J. Adams *et al.*, “Comparison of 15 different stents in superficial femoral arteries by high resolution MRI ex vivo and in vivo,” *J. Magn. Reson. Imaging*, vol. 22, no. 1, pp. 125–135, Jul. 2005.

[35] L. Mertz, “What Is Biocompatibility?: A New Definition Based on the Latest Technology,” *IEEE Pulse*, vol. 4, no. 4, pp. 14–15, Jul. 2013.

[36] C. Trepanier and A. R. Pelton, “Biocompatibility and corrosion resistance of NiTi,” *Nitinol Devices & Components*, pp. 1–9.

[37] C. M. Chan, S. Trigwell, and T. Duerig, “Oxidation of an NiTi alloy,” *Surf. Interface Anal.*,

vol. 15, no. 6, pp. 349–354, 1990.

[38] R. D. Barrett, S. E. Bishara, and J. K. Quinn, “Biodegradation of orthodontic appliances. Part I. Biodegradation of nickel and chromium in vitro,” *Am. J. Orthod. Dentofac. Orthop.*, vol. 103, no. 1, pp. 8–14, Jan. 1993.

[39] S. A. Shabalovskaya, “On the nature of the biocompatibility and on medical applications of NiTi shape memory and superelastic alloys.,” *Biomed. Mater. Eng.*, vol. 6, no. 4, pp. 267–289, 1996.

[40] D. Stoeckel, A. Pelton, and T. Duerig, “We are Nitinol. ™ Self-Expanding Nitinol Stents - Material and Design Considerations Self-Expanding Nitinol Stents - Material and Design Considerations,” vol. 683, 1995.

[41] T. W. Duerig, A. R. Pelton, and D. Stockel, “The utility of superelasticity in medicine.,” *Biomed. Mater. Eng.*, vol. 6, no. 4, pp. 255–266, 1996.

[42] D. Stockel, “Nitinol - A material with unusual properties,” *Endovasc. Updat.*, no. 1, pp. 1–9, 1998.

[43] W. J. Buehler, J. V. Gilfrich, and R. C. Wiley, “Effect of Low-Temperature Phase Changes on the Mechanical Properties of Alloys near Composition TiNi,” *J. Appl. Phys.*, vol. 34, no. 5, pp. 1475–1477, May 1963.

[44] T. W. Duerig and K. N. Melton, “Applications of Shape Memory in the USA Duerig , Melton,” *New Mater. Process. Futur.*, pp. 195–200, 1989.

[45] C. P. Frick *et al.*, “Thermal Processing of Polycrystalline NiTi Shape Memory Alloys,” *MRS Proc.*, vol. 855, 2004.

[46] P. Moine, G. M. Michal, and R. Sinclair, “A morphological study of ‘Premartensitic’ effects

in TiNi," *Acta Metall.*, vol. 30, no. 1, pp. 109–123, 1982.

[47] K. Otsuka, T. Sawamura, and K. Shimizu, "Crystal structure and internal defects of equiatomic TiNi martensite," *Phys. Status Solidi*, vol. 5, no. 2, pp. 457–470, May 1971.

[48] M. H. Elahinia, M. Hashemi, M. Tabesh, and S. B. Bhaduri, "Manufacturing and processing of NiTi implants: A review," *Prog. Mater. Sci.*, vol. 57, no. 5, pp. 911–946, 2012.

[49] T. Waitz, T. Antretter, F. D. Fischer, and H. P. Karnthaler, "Size effects on martensitic phase transformations in nanocrystalline NiTi shape memory alloys," *Mater. Sci. Technol.*, vol. 24, no. 8, pp. 934–940, Aug. 2008.

[50] S. W. Robertson, A. R. Pelton, and R. O. Ritchie, "Mechanical fatigue and fracture of Nitinol," *Int. Mater. Rev.*, vol. 57, no. 1, pp. 1–37, 2012.

[51] T. B. Massalski, H. Okamoto, P. R. Subramanian, and L. Kacprzak, *Binary alloy phase diagrams*, 2nd ed. OH, USA: ASM International, 1990.

[52] J. A. Shaw, C. B. Churchill, and M. A. Iadicola, "Tips and tricks for characterizing shape memory alloy wire: Part 1-differential scanning calorimetry and basic phenomena," *Exp. Tech.*, vol. 32, no. 5, pp. 55–62, 2008.

[53] E. Hornbogen, "Surface Upheavals, Pseudo Martensite, and Martensite Ghosts," *Pract. Metallogr.*, vol. 42, no. 9, pp. 445–453, Sep. 2005.

[54] K. Otsuka and C. Wayman, *Shape Memory Materials*. Cambridge University Press, 1999.

[55] D. C. Lagoudas, *Shape Memory Alloys*, vol. 1. Boston, MA: Springer US, 2008.

[56] G. B. KAUFFMAN and I. MAYO, "The Story of Nitinol: The Serendipitous Discovery of the Memory Metal and Its Applications," *Chem. Educ.*, vol. 2, no. 2, pp. 1–21, 1997.

[57] T. W. Duerig, *Engineering aspects of shape memory alloys*. 1990.

[58] T. H. Nam, T. Saburi, and K. Shimizu, “Cu-Content Dependence of Shape Memory Characteristics in Ti-Ni-Cu Alloys,” *Materials Transactions Jim*, vol. 31, no. 11. pp. 959–967, 1990.

[59] H. C. Ling and K. Roy, “Stress-Induced Shape Changes and Shape Memory in the R and Martensite Transformations in Equiatomic NiTi,” *Metall. Trans. A*, vol. 12, no. 12, pp. 2101–2111, 1981.

[60] D. Stoeckel, “The Shape Memory Effect - Phenomenon, Alloys, and Applications,” *Shape Mem. Alloy. Power Syst. EPRI*, pp. 1–13, 1995.

[61] “CONSTITUTIVE MODELING OF SHAPE MEMORY ALLOYS.” .

[62] R. F. Hamilton, H. Sehitoglu, Y. Chumlyakov, and H. J. Maier, “Stress dependence of the hysteresis in single crystal NiTi alloys,” *Acta Mater.*, vol. 52, no. 11, pp. 3383–3402, 2004.

[63] R. R. Pezarini *et al.*, “On the use of photothermal techniques to study NiTi phase transitions,” *Mater. Res. Express*, vol. 1, no. 2, p. 26502, 2014.

[64] J. Hu, “Investigation on the Cyclic Response of Superelastic Shape Memory Alloy (SMA) Slit Damper Devices Simulated by Quasi-Static Finite Element (FE) Analyses,” *Materials (Basel).*, vol. 7, no. 2, pp. 1122–1141, Feb. 2014.

[65] P. Sittner, Y. Liu, and V. Novak, “On the origin of Lüders-like deformation of NiTi shape memory alloys,” *J. Mech. Phys. Solids*, vol. 53, no. 8, pp. 1719–1746, Aug. 2005.

[66] A. R. Pelton, J. Dicello, and S. Miyazaki, “Optimisation of processing and properties of medical grade Nitinol wire,” *Minim. Invasive Ther. Allied Technol.*, vol. 9, no. 2, pp. 107–118, 2000.

[67] K. Otsuka and K. Shimizu, “Pseudoelasticity and shape memory effects in alloys,” *Int. Met.*

Rev., vol. 31, no. 1, pp. 93–114, 1986.

[68] W. T. Silfvast, "Laser Fundamentals," *American Journal of Physics*, vol. 65, no. 9. p. 932, 1997.

[69] W. M. Steen and J. Mazumder, *Laser Material Processing*. 2010.

[70] A. L. Schawlow and C. H. Townes, "Infrared and optical masers," *Phys. Rev.*, vol. 112, no. 6, pp. 1940–1949, 1958.

[71] T. Tschudi, "K. Thyagarajan, A. K. Ghatak: Lasers, Theory and Applications. Plenum Press, New York 1981. Preis: $ 39.50.," *Berichte der Bunsengesellschaft für Phys. Chemie*, vol. 86, no. 6, pp. 575–575, Jun. 1982.

[72] R. E. Slusher, "Laser technology," *Rev. Mod. Phys.*, vol. 71, no. 2, pp. S471--S479, Mar. 1999.

[73] B. Tam, M. I. Khan, and Y. Zhou, "Mechanical and Functional Properties of Laser-Welded Ti-55.8 Wt Pct Ni Nitinol Wires," *Metall. Mater. Trans. A*, vol. 42, no. 8, pp. 2166–2175, 2011.

[74] M. I. Khan, A. Pequegnat, and Y. N. Zhou, "Multiple memory shape memory alloys," *Adv. Eng. Mater.*, vol. 15, no. 5, pp. 386–393, 2013.

[75] W. Tang, "Thermodynamic study of the low-temperature phase B19′ and the martensitic transformation in near-equiatomic Ti-Ni shape memory alloys," *Metall. Mater. Trans. A*, vol. 28, no. 3, pp. 537–544, 1997.

[76] J. Frenzel, E. P. George, A. Dlouhy, C. Somsen, M. F. X. Wagner, and G. Eggeler, "Influence of Ni on martensitic phase transformations in NiTi shape memory alloys," *Acta Mater.*, vol. 58, no. 9, pp. 3444–3458, 2010.

[77] A. Pequegnat, M. Daly, J. Wang, Y. Zhou, and M. I. Khan, “Dynamic actuation of a novel laser-processed NiTi linear actuator,” *Smart Mater. Struct.*, vol. 21, no. 9, p. 94004, Sep. 2012.

[78] H. C. Man, Z. D. Cui, and T. M. Yue, “Corrosion properties of laser surface melted NiTi shape memory alloy,” *Scr. Mater.*, vol. 45, no. 12, pp. 1447–1453, 2001.

[79] M. I. Khan and Y. Zhou, “Effects of local phase conversion on the tensile loading of pulsed Nd: YAG laser processed Nitinol,” *Mater. Sci. Eng. A*, vol. 527, no. 23, pp. 6235–6238, 2010.

[80] Q. Meng, Y. Liu, H. Yang, B. S. Shariat, and T. H. Nam, “Functionally graded NiTi strips prepared by laser surface anneal,” *Acta Mater.*, vol. 60, no. 4, pp. 1658–1668, 2012.

[81] A. Falvo, F. M. Furgiuele, and C. Maletta, “Laser welding of a NiTi alloy: Mechanical and shape memory behaviour,” *Mater. Sci. Eng. A*, vol. 412, no. 1–2, pp. 235–240, 2005.

[82] C. Maletta, A. Falvo, F. Furgiuele, G. Barbieri, and M. Brandizzi, “Fracture behaviour of nickel-titanium laser welded joints,” *J. Mater. Eng. Perform.*, vol. 18, no. 5–6, pp. 569–574, 2009.

[83] Y. Ogata, M. Takatugu, T. Kunimasa, K. Uenishi, and K. F. Kobayashi, “Tensile Strength and Pseudo-elasticity of YAG Laser Spot Melted Ti-Ni Shape Memory Alloy Wires,” *Mater. Trans.*, vol. 45, no. 4, pp. 1070–1076, 2004.

[84] a Tuissi, S. Besseghini, T. Ranucci, F. Squatrito, and M. Pozzi, “Effect of Nd-YAG laser welding on the functional properties of the Ni–49.6at.%Ti,” *Mater. Sci. Eng. A*, vol. 273–275, pp. 813–817, 1999.

[85] P. Schlossmacher, T. Haas, and A. S. Ussler, “Laser-Welding of a Ni-Rich TiNi Shape

Memory Alloy : Mechanical Behavior To cite this version :," vol. 7, no. 1 997, pp. 0–5, 1997.

[86] Sudheer Ambekar and Anil Nanda, "Charles Stent and the mystery behind the word 'stent,'" *J. Neurosurg.*, vol. 119, no. 3, pp. 774–777, 2013.

[87] S. Deora, "The story of 'STENT': From noun to verb.," *Indian heart journal*, vol. 68, no. 2. India, pp. 235–237, 2016.

[88] J. H. C. Reiber, "Handbook of coronary stents. Patrick Serruys, M.D., editor.," *Int. J. Card. Imaging*, vol. 13, no. 4, p. 360, 1997.

[89] A. S. Taylor, P. W. Stratford, Y. P. Yianni, and M. J. Woodroffe, "Braided stent." Google Patents, 2000.

[90] S. Zhao, X. (Cheryl) Liu, and L. Gu, "The Impact of Wire Stent Fabrication Technique on the Performance of Stent Placement," *J. Med. Device.*, vol. 6, pp. 11007-1-11007–4, 2012.

[91] O. Çakir, H. Temel, and M. Kiyak, "Chemical etching of Cu-ETP copper," *J. Mater. Process. Technol.*, vol. 162–163, no. SPEC. ISS., pp. 275–279, 2005.

[92] D. M. Allen, "Progress towards Clean Technology for Photochemical Machining," *CIRP Ann. - Manuf. Technol.*, vol. 42, no. 1, pp. 197–200, 1993.

[93] S. B. G, "Liquid cutting of hard materials." Google Patents, 1961.

[94] F. N. C, "High velocity liquid jet." Google Patents, 1970.

[95] N. B. Dahotre, *Laser Fabrication and Machining of Materials*, vol. 33. Springer, 2012.

[96] J. Powell, *CO2 Laser Cutting*. London: Springer London, 1998.

[97] W. P. . Jüptner, "LIA handbook of laser materials processing," *Opt. Lasers Eng.*, vol. 38, no. 6, pp. 608–610, 2002.

[98] D. Schuöcker, *High Power Lasers in Production Engineering*. Imperial College Press, 1999.

[99] J. F. Ready, *Industrial applications of lasers*. Academic Press, 1997.

[100] P. Di Pietro and Y. L. Yao, "An investigation into characterizing and optimizing laser cutting quality — A review," *Int. J. Mach. Tools Manuf.*, vol. 34, no. 2, pp. 225–243, Feb. 1994.

[101] Y. P. Kathuria, "The potential of biocompatible metallic stents and preventing restenosis," *Mater. Sci. Eng. A*, vol. 417, no. 1–2, pp. 40–48, Feb. 2006.

[102] I. Decker, J. Ruge, and U. Atzert, "Physical Models And Technological Aspects Of Laser Gas Cutting," *Proc. SPIE*, vol. 455. pp. 81–87, 1984.

[103] K. Chen, Y. L. Yao, and V. Modi, "Numerical simulation of oxidation effects in the laser cutting process," *Int. J. Adv. Manuf. Technol.*, vol. 15, no. 11, pp. 835–842, 1999.

[104] D. Havrilla, *Process Fundamentals of Industrial Laser Welding and Cutting*, no. August. 2002.

[105] S. M. Shariff, G. Sundararajan, and S. V. Joshi, "Parametric influence on cut quality attributes and generation of processing maps for laser cutting," *J. Laser Appl.*, vol. 11, no. 2, p. 54, 1999.

[106] J. Meijer, "Laser beam machining (LBM), state of the art and new opportunities," *J. Mater. Process. Technol.*, vol. 149, no. 1–3, pp. 2–17, 2004.

[107] J. E. Geusic, H. M. Marcos, and L. G. Van Uitert, "LASER OSCILLATIONS IN Nd-DOPED YTTRIUM ALUMINUM, YTTRIUM GALLIUM AND GADOLINIUM GARNETS," *Appl. Phys. Lett.*, vol. 4, no. 10, pp. 182–184, May 1964.

[108] C. Wandera and V. Kujanpää, “Optimization of parameters for fibre laser cutting of a 10 mm stainless steel plate,” *Proc. Inst. Mech. Eng. Part B J. Eng. Manuf.*, vol. 225, no. 5, pp. 641–649, May 2011.

[109] Anping Liu and Kenichi Ueda, “The absorption characteristics of circular, offset, and rectangular double-clad fibers,” *Opt. Commun.*, vol. 132, no. 5–6, pp. 511–518, Dec. 1996.

[110] M. Tsuji, “IPG fibre lasers and aluminium welding applications,” *Weld. Int.*, vol. 23, no. 10, pp. 717–722, Oct. 2009.

[111] P. U. Weiss, “Hot flashes, cold cuts:ultrafast lasers give power tools a new edge,” *The Free Library*, 2002. [Online]. Available: https://www.thefreelibrary.com/Hot flashes, cold cuts: ultrafast lasers give power tools a new edge-a094774392. [Accessed: 13-Feb-2017].

[112] J. Meijer *et al.*, “Laser Machining by short and ultrashort pulses, state of the art and new opportunities in the age of the photons,” *CIRP Ann. - Manuf. Technol.*, vol. 51, no. 2, pp. 531–550, 2002.

[113] A. Lamikiz, L. N. L. De Lacalle, J. A. Sánchez, D. Del Pozo, J. M. Etayo, and J. M. López, “CO2 laser cutting of advanced high strength steels (AHSS),” *Appl. Surf. Sci.*, vol. 242, no. 3–4, pp. 362–368, 2005.

[114] L. Shanjin and W. Yang, “An investigation of pulsed laser cutting of titanium alloy sheet,” *Opt. Lasers Eng.*, vol. 44, no. 10, pp. 1067–1077, 2006.

[115] A. Cekic, D. Begic-Hajdarevic, M. Kulenovic, and A. Omerspahic, “CO2 Laser Cutting of Alloy Steels Using N2 Assist Gas,” *Procedia Eng.*, vol. 69, pp. 310–315, 2014.

[116] N. Rajaram, J. Sheikh-Ahmad, and S. H. Cheraghi, “CO2 laser cut quality of 4130 steel,” *Int. J. Mach. Tools Manuf.*, vol. 43, no. 4, pp. 351–358, 2003.

[117] N. Rajaram and S. H. Cheraghi, “Parametric Study of the Effect of Feed Speed and Power on Laser Cut Quality of 4130 Steel,” no. May 2002, 2014.

[118] B. S. Yilbas, “Laser cutting quality assessment and thermal efficiency analysis,” *J. Mater. Process. Technol.*, vol. 155–156, pp. 2106–2115, 2004.

[119] L. Li, M. Sobih, and P. L. Crouse, “Striation-free Laser Cutting of Mild Steel Sheets,” *{CIRP} Ann. - Manuf. Technol.*, vol. 56, no. 1, pp. 193–196, 2007.

[120] E. Kannatey-Asibu, *Principles of Laser Materials Processing*. Wiley, 2009.

[121] S. J. Lv, Y. Wang, and S. J. Ji, “Quality Analysis of Pulsed Laser Cutting of Superalloy Sheet,” *Key Eng. Mater.*, vol. 315–316, pp. 113–117, 2006.

[122] Y. Zhou *et al.*, “Origin of 2-stage R-phase transformation in low-temperature aged Ni-rich Ti-Ni alloys,” *Acta Mater.*, vol. 53, no. 20, pp. 5365–5377, 2005.

[123] F. Jiang, Y. Liu, H. Yang, L. Li, and Y. Zheng, “Effect of ageing treatment on the deformation behaviour of Ti-50.9 at.% Ni,” *Acta Mater.*, vol. 57, no. 16, pp. 4773–4781, 2009.

[124] G. Fan, W. Chen, S. Yang, J. Zhu, X. Ren, and K. Otsuka, “Origin of abnormal multi-stage martensitic transformation behavior in aged Ni-rich Ti-Ni shape memory alloys,” *Acta Mater.*, vol. 52, no. 14, pp. 4351–4362, 2004.

[125] Y. Zhou *et al.*, “Understanding of multi-stage R-phase transformation in aged Ni-rich Ti-Ni shape memory alloys,” *Mater. Sci. Eng. A*, vol. 438–440, no. SPEC. ISS., pp. 602–607, 2006.

[126] M. I. Khan, “Pulsed Nd : YAG Laser Processing of Nitinol,” 2011.

[127] J. Wang, “Multiple Memory Material Processing for Augmentation of Local

Pseudoelasticity and Corrosion Resistance of NiTi-based Shape Memory Alloys," 2013.

[128] C. Momma, U. Knop, and S. Nolte, "Laser cutting of slotted tube coronary stents—state-of-the-art and future developments," *Prog. Biomed. Res.*, vol. 4, no. February, pp. 39–44, 1999.

[129] Y. P. Kathuria, "An overview on laser microfabrication of bicompatible metallic stent for medical therapy," *Proc. SPIE*, vol. 5399. pp. 234–244, 2004.

[130] Y. P. Kathuria, "Laser microfabrication of biocompatible metallic stent for medical therapy," 2003, p. 176.

[131] Y. P. Kathuria, "Laser microprocessing of metallic stent for medical therapy," *J. Mater. Process. Technol.*, vol. 170, no. 3, pp. 545–550, Dec. 2005.

[132] A. RAVAL, A. CHOUBEY, C. ENGINEER, and D. KOTHWALA, "Development and assessment of 316LVM cardiovascular stents," *Mater. Sci. Eng. A*, vol. 386, no. 1–2, pp. 331–343, Nov. 2004.

[133] J. Dobránszky, Z. Puskás, and G. Meszlényi, "Laser Cutting of High Precision Tubes," in *Materials Science, Testing and Informatics IV*, 2008, vol. 589, pp. 427–431.

[134] L. Chen, "Laser Cutting for Medical Device (Stent) - Yesterday, Today and Tomorrow," in *ICALEO*, 2008, pp. 320–324.

[135] Y. Motemani, M. Nili-Ahmadabadi, M. J. Tan, M. Bornapour, and S. Rayagan, "Effect of cooling rate on the phase transformation behavior and mechanical properties of Ni-rich NiTi shape memory alloy," *J. Alloys Compd.*, vol. 469, no. 1–2, pp. 164–168, Feb. 2009.

[136] X. Liu, Y. Wang, D. Yang, and M. Qi, "The effect of ageing treatment on shape-setting and superelasticity of a nitinol stent," *Mater. Charact.*, vol. 59, no. 4, pp. 402–406, Apr. 2008.

[137] B. Reid, “Heat Treating In Molten Salt,” Georgetown, 1996.

[138] D. Scheinert *et al.*, “Prevalence and clinical impact of stent fractures after femoropopliteal stenting,” *J. Am. Coll. Cardiol.*, vol. 45, no. 2, pp. 312–315, 2005.

[139] I. W. L. Gore & Associates, “Mechanical Properties of Nitinol Stents and Stent-grafts: Comparison of 6mm Diameter Devices,” pp. 1–11, 2007.

[140] A. R. Pelton, V. Schroeder, M. R. Mitchell, X.-Y. Gong, M. Barney, and S. W. Robertson, “Fatigue and durability of Nitinol stents.,” *J. Mech. Behav. Biomed. Mater.*, vol. 1, no. 2, pp. 153–164, Apr. 2008.

[141] J.-P. Nuutinen, C. Clerc, and P. Törmälä, “Theoretical and experimental evaluation of the radial force of self-expanding braided bioabsorbable stents,” *J. Biomater. Sci. Polym. Ed.*, vol. 14, no. 7, pp. 677–687, 2003.

[142] R. Rieu *et al.*, “Radial force of coronary stents: a comparative analysis.,” *Catheter. Cardiovasc. Interv.*, vol. 46, no. April 1998, pp. 380–391, 1999.

[143] A. Michael, Y. N. Zhou, and M. I. Khan, “Novel method to analyse tensile properties of ultra-fine NiTi wires with a visual extensometer,” *Mater. Lett.*, vol. 182, pp. 177–180, 2016.

[144] J. E. Schaffer, “Structure-Property Relationships in Conventional and Nanocrystalline NiTi Intermetallic Alloy Wire,” vol. 18, no. August, pp. 582–587, 2009.

[145] Q. P. Sun and Y. J. He, “A multiscale continuum model of the grain-size dependence of the stress hysteresis in shape memory alloy polycrystals,” vol. 45, pp. 3868–3896, 2008.

[146] A. Runciman, D. Xu, A. R. Pelton, and R. O. Ritchie, “An equivalent strain/Coffin-Manson approach to multiaxial fatigue and life prediction in superelastic Nitinol medical devices.,” *Biomaterials*, vol. 32, no. 22, pp. 4987–4993, Aug. 2011.